

**TERAHERTZ SPECTROSCOPY OF NITRIC OXIDE FOR EMISSIONS MONITORING IN
BIOENERGY SYSTEMS**

by

Ahmed Adel Nasreldin Mohamed

B.Sc., University of Ain-Shams, Egypt, 2007

THESIS SUBMITTED IN PARTIAL FULFILLMENT OF
THE REQUIREMENTS FOR THE DEGREE OF
MASTER OF SCIENCE
IN
PHYSICS

UNIVERSITY OF NORTHERN BRITISH COLUMBIA

(March) 2017

© Ahmed Nasr Mohamed, 2017

Abstract

The aim of this thesis is to study pollutants that are emitted from combustion systems using Terahertz time domain spectroscopy (THz-TDS). In particular, this thesis will focus on Nitric Oxide (NO), which is present in flue gases and contributes to air pollution. It is also interesting from a Physics perspective because it contains an unpaired electron in the valence shell, which leads to a complicated energy level structure, and interesting Physics.

In this thesis, we aim to answer the question: “what is the detection limit of NO, using THz-TDS, and is it suitable for industrial emissions monitoring?” It is therefore necessary to look at detection limits, which in turn requires conducting THz spectroscopy at different gas pressures.

A gas-cell containing NO is used in a THz-TDS set-up, where the temporal and spectral response of a THz pulse propagating through a gas sample of NO molecules is probed. A theoretical model for the interaction between the THz radiation and NO is developed, taking into account the complicated molecular structure of NO. A direct comparison is then made between the experimental data and our theoretical model. The good agreement between theory and experiment allows us to project the limits of detection for NO sensing that is possible with commercially available THz systems today, and the potential for the technology to be used in harsh environments is discussed.

List of papers

- 1- “Terahertz spectroscopy of wood and combustion gas,” M. Reid, T. Inagaki, S. Tsuchikawa, K. Lawyer, B. Ahmed, A. Nasr Mohamed, E. T. Jensen, and I.D. Hartley. Invited presentation at the Canadian Association of Physics Congress, Sudbury, ON, CAN (Wednesday, June 18, 2014) [53].

- 2- “THz NDE and applications for sensing and imaging of wood products,” M. Reid, I. Hartley, E. Jensen, P. Kilcullen, B. Ahmed, A. Nasr Mohamed, and K. Lawyer, Invited departmental seminar, Graduate Agricultural School, Nagoya University, Japan (Nov. 4, 2016) [54].

Table of Contents

Abstract	-----	II
List of papers	-----	III
Table of contents	-----	IV
List of figures	-----	VI
List of tables	-----	VIII
List of abbreviations	-----	IX
Acknowledgment	-----	X
1. Introduction	-----	1
2. Historical background	-----	3
2.1 Recent methods of detection of nitric oxide	-----	6
2.2 Terahertz portion of the electromagnetic spectrum	-----	10
2.3 THz time-domain spectroscopy	-----	13
2.4 Generation and detection of THz pulses	-----	13
3. Rotational spectroscopy model of nitric oxide	-----	18
3.1 Model for NO	-----	18

4.	Experimental setup and results	29
4.1	Experimental setup	29
4.2	Fitting the data to the model	37
4.2.1	Fitting for the refractive index n	38
4.2.2	Fitting of the rotational constant B_v	39
4.2.3	Fitting of the time constant τ_c	42
4.2.4	Statistical error estimations and analysis	43
4.2.5	Comparison of model and experimental data	45
4.3	Pressure scaling	47
4.4	Experimental results and analysis	50
4.4.1	The results of the rotational constants $B_0^{1/2}$ and $B_0^{3/2}$	53
4.4.2	The results of the angular frequency linewidth	58
4.5	Future work	69
5.	Conclusion	72
	References	75
	Appendix	81

List of figures

Figure 1 Terahertz spectral region	-----	10
Figure 2 THz absorption and transmitted spectrum through methyl halide vapors	-----	11
Figure 3 Photoconductive THz emitter	-----	15
Figure 4 Molecular orbital diagram of NO in the electronic ground state	-----	19
Figure 5 Diatomic molecule as a rigid rotor	-----	26
Figure 6 Menlo system setup	-----	30
Figure 7 Example of THz waveform in time and frequency domains	-----	32
Figure 8 The time domain response for NO at a partial pressure of $p = 750$ mmHg	-----	33
Figure 9 The frequency domain response for NO at a partial pressure of $p = 750$ mmHg	---	34
Figure 10 Absorbance spectrum of NO at a partial pressure of $p = 750$ mmHg	-----	36
Figure 11 Fitting of the refractive index n	-----	38
Figure 12 Fitting statistics of the rotational constant $B_0^{1/2}$	-----	39
Figure 13 Fitting statistics of the rotational constant $B_0^{3/2}$	-----	40
Figure 14 Fitting model for the angular frequency $\Delta\omega$	-----	42

Figure 15	Fitting of $B_0^{1/2}$ at a partial pressure of $p = 750$ mmHg with statistical error	-----	44
Figure 16	THz scan of NO at a partial pressure of $p = 525 \pm 5\%$ mmHg	-----	45
Figure 17	Residual between model and data	-----	46
Figure 18	Schematic diagram for NO and N ₂ gas mixing	-----	49
Figure 19	A long 200 ps scan for NO at atmospheric pressure (760 mmHg)	-----	51
Figure 20	THz scan at 100 mmHg, showing echoes for 100, 450 and 750 mmHg	-----	52
Figure 21	The change in $B_0^{1/2}$ with respect to pressure change	-----	54
Figure 22	The change in $B_0^{3/2}$ with respect to pressure change	-----	55
Figure 23	The change in $B_0^{1/2}$ and $B_0^{3/2}$ with respect to pressure change	-----	57
Figure 24	The change in $\Delta\omega$ with respect to pressure change	-----	59
Figure 25	The change in $\Delta\omega$, $\Delta\omega_{1/2}$ and $\Delta\omega_{3/2}$ with respect to pressure change	-----	60
Figure 26	Example of NO at low and high pressure	-----	64
Figure 27	The change of the height of the third echo with pressure	-----	67
Figure 28	Inset for the change of the height of the third echo with pressure	-----	68

List of tables

Table 1	Some examples of Nitrogen Oxides (NO _x)	-----	4
Table 2	Summary of methods for detecting Nitric Oxide	-----	9
Table 3	Some examples of published literature values of $B_0^{1/2}$ and $B_0^{3/2}$	-----	41
Table 4	The rotational constant change with NO partial pressure	-----	53
Table 5	The change in the angular frequency with the change of NO pressure	-----	58
Table 6	Total collision cross-sections for NO and N ₂	-----	63
Table 7	The peak-to-peak ratio of the 3 rd echo with the change of NO partial pressure	-----	66

List of abbreviations

NO	Nitric Oxide.
VOCs	Volatile Organic Compounds.
FIR	Far infrared.
SNR	Signal-to-noise ratio.
THz-TDS	Terahertz time-domain spectroscopy.
CCN	Cloud Condensation Nuclei.
QCL	Quantum Cascade Lasers.
Ppm	Parts-per-million.
Ppb	Parts-per-billion.
Ppt	Parts-per-trillion.
FID	Free Induction Decay.
FWHM	Full Width at Half Maximum.
B_v	The rotational constant of the vibrational state v .
D_v	The centrifugal stretching constant (distortion constant).
μ	The electric dipole moment.
τ_c	The collisional time constant.
SSE	Sum of Squared Error.
RMS	Root Mean Square.
FTS	Fourier transform spectroscopy.

Acknowledgment

I would like to express my deep gratitude to my research supervisor, Dr. Matthew Reid for giving me the opportunity to do research and providing invaluable guidance throughout this research. His dynamism, vision, sincerity and motivation have deeply inspired me. He has taught me the methodology to carry out the research and to present the research work as clearly as possible. It was a great privilege and honor to work and study under his guidance. I am extremely grateful for what he has offered me. I would also like to thank him for his friendship, empathy, and great sense of humor.

And special and deep thanks to Dr. Erik Jensen for his support during my experimental work. Also I would like to thank Dr. Ian Hartley and Dr. George Jones for giving me a great sense of humor and love during my study at UNBC.

I am extremely grateful to my family for their love, understanding, prayers and continuing support to complete this research work. Also, I would like to say thanks to my friends and research colleagues Bilal Ahmed, Patrick Kilcullen, and Kim Lawyer for their support and help during my research time.

Chapter 1

Introduction

The main thrust of my thesis work is to study pollutants that are emitted from combustion systems, specifically Nitric Oxide (NO), using Terahertz (THz) spectroscopy. THz spectroscopy has strong potential for sensing applications involving molecules with a permanent dipole moment as the entire manifold of thermally populated rotational energies can be probed within the bandwidth of a typical THz pulse (which is usually about 3 THz).

Nitric Oxide, which is present in flue gases and contributes to air pollution from combustion systems, was chosen as it is also interesting from a Physics perspective because it contains an unpaired electron in the valence shell, which leads to a complicated energy level structure in comparison to CO, for example, which was previously studied in the THz research lab at UNBC [1]. The primary goal of this thesis will be to answer the question: “what is the detection limit of NO gas using THz technology, and is it suitable for industrial emissions monitoring?” In order to answer this question, it will be necessary to look at detection limits, which in turn requires conducting THz spectroscopy at different gas pressures.

We will develop a model of the interaction between a THz field and NO molecules, following the work previously conducted by Grischkowsky [2], but extending it to the more complicated NO molecule. This will be used to examine the pressure scaling, and compared to experimental data to determine limits of detection.

In Chapter 1 and Chapter 2, background related to this project is presented to put the work into context, followed by a description of how we implemented a THz-TDS system for detection of NO gas. In Chapter 3, the model of the interaction between THz radiation and NO molecules at a specific temperature and pressure is presented. The THz propagation through NO is calculated using the Matlab® programming language by numerically implementing the theoretical model. In Chapter 4, experimental results for THz-TDS of NO at atmospheric pressure will be presented. Then, by using the Matlab programming environment, experimental data and the theoretical model are compared.

Results are presented for NO partial pressures in the range of 100 mmHg – 750 mmHg, and a total pressure of atmospheric pressure (approximately 760 mmHg) by mixing with N₂ up to atmospheric pressure. Finally, the results are analyzed and discussed, and the theoretical model for the THz time-domain response of NO molecules is compared to experimental data at different pressures. We tested the validity of the model, and found experimental values for the rotational constant and collisional time constant of NO using THz-TDS which are shown to be consistent with published literature values. Then, the results are used to project the ultimate limit of detection for commercially available THz systems.

Chapter 2

Historical background

Air pollution is an important issue at present, especially for the Prince George region because of a long history of poor air quality and significant industrial emissions. In addition, air pollution has had a dramatic effect on the climate in the last century, which in turn, has significant implications for human health. There are many sources of air pollution such as the emissions from vehicles, industrial activities, and combustion systems in general, all of which produce pollutant gases and particulate.

There are different types of pollution which can be categorized according to its type and its effect, including smoke (and associated particulate matter), ash, SO_x , NO_x , CO, VOCs, and others. Nitrogen Oxides (NO_x) are a very interesting and important family of air-polluting chemical compounds. Much attention has been devoted to NO because of its toxicity and also due to its possible effects on neurotransmitters, where NO is synthesized by NO-synthase (an enzyme that catalyzes a synthesis process), then NO molecules simply diffuse from nerve terminals, which causes harm to the human body by changing the brain chemistry [3].

NO also transforms easily into nitrogen dioxide (NO₂), which has negative health effects associated with it. The small size of NO makes it diffusible in both aqueous and lipid environments which allows rapid spreading even through membranes [4]. Furthermore, NO is a minor constituent of Earth's atmosphere with a prominent role in the catalytic decomposition of ozone in the stratosphere [5]. The decomposition of the ozone layer increases the amount of ultraviolet radiation received at the surface of the earth, which has harmful effects on human health (causing such diseases as skin cancer and cataracts) as well as negative effects on the environment (climate change for example) [6].

Diatomic molecular nitrogen (N₂) is an inert gas that makes up about 80% of the air we breathe. However, the chemical element nitrogen (N), as a single atom, is highly reactive exhibiting ionization levels from +1 to +5, which allows the formation of several different oxides [7]. The family of NO_x compounds and their properties are listed in Table 1 [7].

Table 1. Some examples of Nitrogen Oxides (NO_x)

Formula	Name	Nitrogen Valence	Properties
N ₂ O	Nitrous Oxide	1	colorless gas, water soluble
NO N ₂ O ₂	Nitric Oxide Dinitrogen Dioxide	2	colorless gas slightly water soluble
N ₂ O ₃	Dinitrogen Trioxide	3	black solid, water soluble, decomposes in water
NO ₂ N ₂ O ₄	nitrogen dioxide dinitrogen tetroxide	4	red-brown gas, very water soluble, decomposes in water
N ₂ O ₅	dinitrogen pentoxide	5	white solid, very water soluble, decomposes in water

NO is formed in high temperature combustion and is easily oxidized to NO₂, which reacts to form nitrates. When rain forms around certain types of pollutants, such as NO and SO₂, raindrops condense around microscopic pieces of material called Cloud Condensation Nuclei (CCN). The sulphate and nitrate particles (< 1µm) can act as CCN, resulting in acid rain [8]. Visibility can also be reduced by the presence of such particles (especially by sulphate and nitrate particles).

NO has two distinct electronic energy states resulting in far-infrared rotational absorption spectra having two distinct manifolds of rotational energies, one for each electronic state. The distinct electronic states result from spin-orbit coupling of the single unpaired valence electron [9].

NO is polar with a permanent dipole moment, which comes about because oxygen has a higher electronegativity than nitrogen, and gives the molecule an intrinsic electric dipole moment. This dipole interacts strongly with radiation whose frequencies lie in the far-infrared [10].

Furthermore, NO is unique in having an excited electronic state NO(²Π_{3/2}) so near (123 cm⁻¹) to the ground electronic state NO(²Π_{1/2}) such that it is appreciably populated at room temperature [11]. These two molecular electronic states (²Π_{1/2} and ²Π_{3/2}) derive their labels from the well-known atomic orbital *s*, *p*, *d*, and *f* nomenclature, where instead, molecular states are labeled as Σ, Π, Δ, and φ, corresponding to a molecular orbital angular momentum of $\ell = 0, 1, 2,$ and $3,$ respectively.

These two molecular electronic states are created because of the Spin-Orbit coupling, which is an effect of how the spin angular momentum of the electron and the orbital angular momentum add to give a total angular momentum $J (=s+\ell)$. J therefore has contributions from spin angular momentum s and orbital angular momentum ℓ , so that J can take on values of $1/2$ or $3/2$, leading to the two different states (${}^2\Pi_{1/2}$) and (${}^2\Pi_{3/2}$). These two states, each with their own rotational manifold of absorption lines, lead to a complicated pure rotational spectrum in the far-infrared, for which we will develop a theoretical model and compare to measurements in this thesis.

2.1 Recent methods of detection of nitric oxide

For molecular detection in an atmospheric environment, we can use rotational spectroscopy, where the energies of transitions between quantized rotational states of molecules in the gas phase are measured.

NO is not easily detected in the atmosphere employing rotational spectroscopy because of its small dipole moment of 0.15872 Debye (D) [12]. Detection of NO is also challenging because of its unique chemical and physical properties, including its reactivity (with other chemical components in the air), and rapid diffusion (because of its small size). NO is also highly reactive and rapidly scavenged by endogenous compounds including oxygen (O_2), heme-proteins (e.g. hemoglobin) and others. This reactivity causes NO to have a short half-life (few seconds), thus complicating its detection in the atmosphere [13].

These reasons make it difficult to detect NO, so that techniques with a wide dynamic response range are required [13]. High-resolution IR spectroscopy of its fundamental band is commonly used, which allow us to measure NO concentrations as low as 0.01 parts per million (ppm) in a gas volume of 1 cm³ in a time of ~ 4 seconds [14].

Several methods have been developed to detect NO based on the rotational transitions, including far-infrared (FIR) spectroscopy and photoacoustic spectroscopy. These two techniques are sensitive enough to detect tens of (ppm) of NO pollution in air [14].

The first technique, FIR spectroscopy, relies on the fact that NO molecular rotational energies lie in the FIR portion of the electromagnetic spectrum, and typically rely on FIR radiation produced using Quantum Cascade Lasers (QCLs), which are small semiconductor lasers that emit light in the mid- and far-infrared portion of the electromagnetic spectrum. These sources can be tuned to specific wavelengths to conduct absorption spectroscopy and probe the characteristic fingerprints of the absorbing molecules for identification and quantification. This technique provides molecular information by measuring vibrational and rotational transitions in NO molecules.

The second technique, photoacoustic spectroscopy, relies on the same principles as absorption spectroscopy, however, the sensitive nature of microphonics is exploited to achieve increased sensitivity when the gas under study absorbs laser light at particular wavelengths via molecular transitions causing acoustic modes inside the sample cell to be excited.

The absorbed energy induces local heating, which can in turn generate a pressure wave and a faint acoustic signal [15], which can be detected with high sensitivity using microphones. Photoacoustic spectroscopy is a useful technique for monitoring chemical composition because the detection limit scales favorably with miniaturization. Also, in photoacoustic spectroscopy the signal is increased by miniaturization because the coupling of temperature to pressure is inversely proportional to volume [16].

In fact, many industrially relevant gases such as carbon sulfide, carbon monoxide, nitrogen monoxide, carbonyl sulfide, and others, have absorption lines in this portion of the spectrum [17]. That is, each gas has a unique set of absorption lines related to the molecular structure through the allowed rotational (and vibrational) energies of the molecule.

In FIR spectroscopy, light of different wavelengths is passed through a sample of gas, and these absorption lines are mapped in frequency to extract the fingerprints, which can then be used for identification and quantification. There are several methods that can be used for performing FIR spectroscopy. Fourier transform spectroscopy (FTS) is perhaps the most common technique used for studying molecular resonances [18].

A survey of methods for detecting NO, collected from the literature, is presented below in Table 2. The typical limits of detection are in the single ppb (part per billion), or ppm (parts-per-million) range.

Table 2. Summary of methods for detecting NO, and their respective detection limits.

Method Name	Detection Limit
Spectroscopic chemiluminescence Luminal/H ₂ O ₂ -based [19]	0.3 ppb
Spectroscopic of NO by fluorescence and chemiluminescence [20]	5 ppm (in Nitrogen atmosphere)
QEPAS system was demonstrated using an external-cavity (QCL) [21]	15 ppb
Tunable external cavity (QCL)- based detection [22]	96 ppb
Photoacoustic detection of NO with a Helmholtz resonant (QCL) [23]	100 ppb
Conventional photoacoustic spectroscopy systems [24]	500 ppb
Quartz-enhanced photoacoustic Spectroscopy (QCL-based) [25]	10 ppm (in Nitrogen atmosphere) 2.5ppm (Mixture 80% N ₂ and 20% O ₂)

As can be seen, the majority of the techniques are QCL-based and are conducted in laboratory research environments. The “Quartz-enhanced photoacoustic spectroscopy [25]”, which is considered an applied outdoor technique (in an atmospheric environment), will be used to compare to our final results for limits of detections (as our work is also related to detection of NO in atmospheric environments).

2.2 Terahertz portion of the electromagnetic spectrum

This thesis work employs a new method to detect NO molecules, using THz-TDS. THz-TDS is currently being researched extensively as it is a promising, non-destructive method for testing samples that range from packaged goods to artwork and biological tissues [26]. Terahertz (1 THz = 10^{12} Hz) frequencies, extending from tens of GHz to a few THz, lie in the FIR portion of the electromagnetic spectrum as shown in Figure 1. These frequencies are suitable for probing the rotational absorption lines of many common molecules.

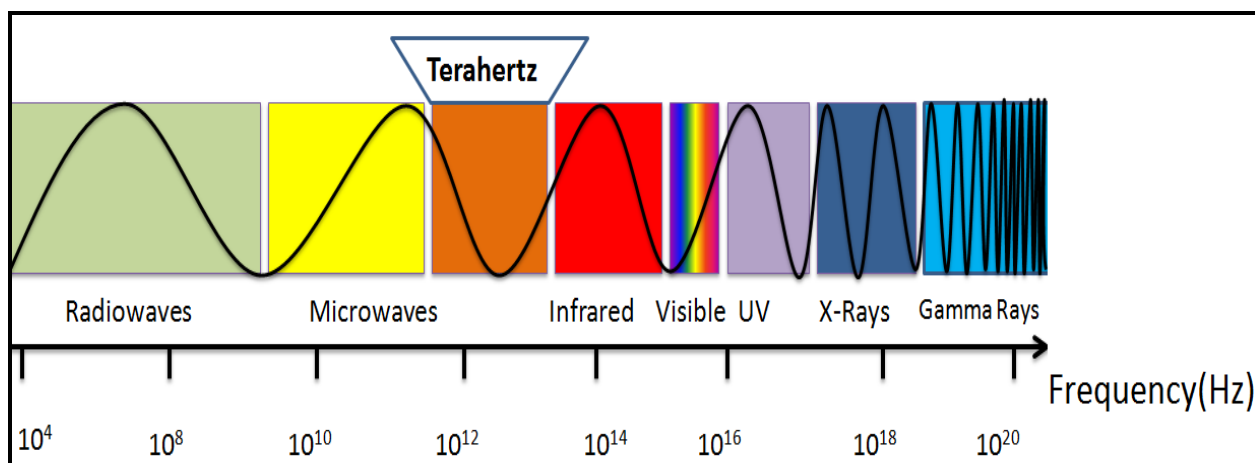


Figure 1. THz spectral region (40GHz to 4THz)

THz-TDS relies on coherent detection of pulsed electromagnetic fields, which measures the electric field directly in the time-domain. THz pulses typically have a large bandwidth (which usually spans a range of 0.1 to several THz) because of being composed of short pulses. As a result, the entire manifold of thermally populated rotational energies of many molecules can be probed simultaneously. What is more, the approximately evenly spaced rotational lines in the frequency domain (a signature of linear diatomic molecules) translate to the radiation of periodic “commensurate echoes” in the time domain. For example, see Figure 2.A and 2.B below [2].

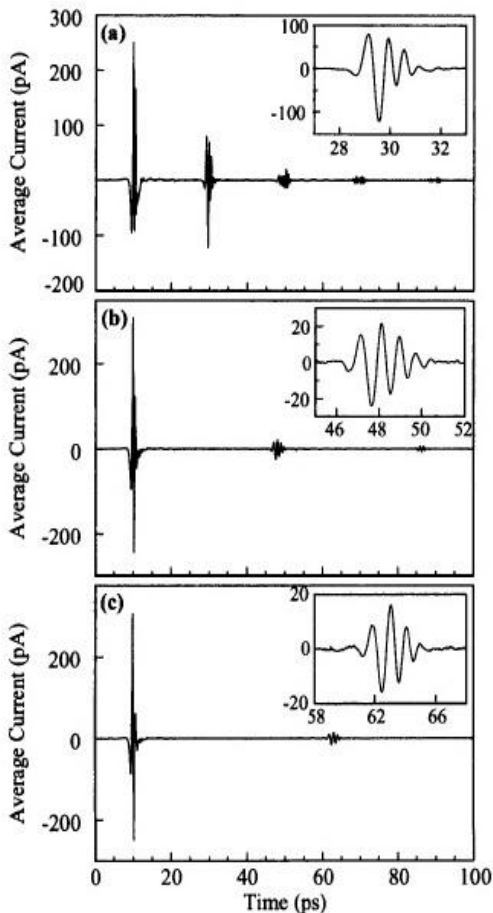


Figure 2.A Measured transmitted THz signal through 2.27 cm of 666 hPa of methyl halide vapors. The insets show the first commensurate echoes on an expanded scale:

(a) methyl fluoride, (b) methyl chloride, (c) methyl bromide.

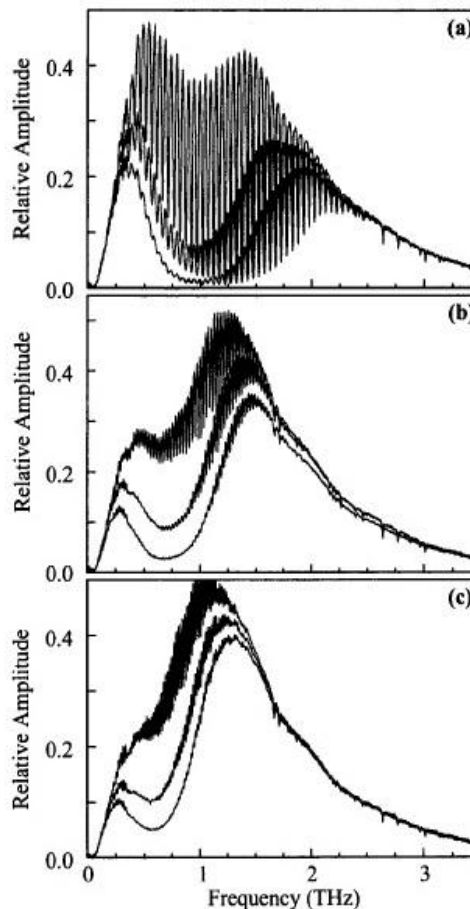


Figure 2.B Measured THz-TDS absorption spectra from the THz pulses transmitted through 2.27 cm of 666, 1333, and 2000 hPa pressures:

(a) methyl fluoride, (b) methyl chloride, (c) methyl bromide.

The propagation of a THz pulse through a molecular vapour simultaneously excites the manifold of rotational transitions (the absorption lines visible in Figure 2.B), thereby causing the molecules to radiate a Free Induction Decay (FID) signal [27].

This rephasing process is manifest as a train of sub-picosecond THz pulses with a repetition rate equal to the inverse of the frequency separation between adjacent rotational absorption lines in the frequency domain. These periodic pulses are termed “THz commensurate echoes” [27].

The measured time-resolved THz echoes carry almost complete information about the molecular system. Molecular constants such as the rotational constant (related to the moment of inertia of the molecule), the centrifugal stretching constant (resulting from increased bond length with increasing rotational energy), as well as the coherence relaxation time dictating the decay time-scale of the echoes, are all reflected in the temporal profile of the transmitted THz signal.

The latter is determined only by collisional dephasing, since Doppler and lifetime broadening are negligible under the conditions studied in our work [2]. Therefore, the time-domain echoes contain information about the molecules present, their amount, as well as the pressure and temperature of the molecular system.

In this thesis, we will develop a theoretical model that predicts the temporal profile of the transmitted THz pulses, which will allow us to make measurements of the key molecular parameters discussed above by fitting experimentally measured transmitted THz signals to the theoretical model. This thesis then aims to exploit the echoes directly in the time domain as *temporal signatures*, to perform characterization of gases in a unique way, different from traditional techniques of absorption spectroscopy, which relies on *spectral signatures*. This is what we will refer to as Terahertz time domain spectroscopy (THz-TDS), which we will describe more fully in the next section of the thesis.

2.3 THz time-domain spectroscopy

THz-TDS was first demonstrated in 1985 by Auston and Cheung at Bell Laboratories [28]. THz-TDS does not measure the frequency-dependent intensity of an electromagnetic wave, but rather, time-dependent electric fields directly. This type of detection is referred to as coherent detection, and these measurements contain both amplitude and phase information allowing the extraction of the full complex dielectric function of materials. This makes THz-TDS much more powerful than traditional frequency domain measurements.

2.4 Generation and detection of THz pulses

There are many ways to generate pulsed THz radiation, however, the most common for THz-TDS is using photoexcited carrier transport (photoconductive antennas for example) [29]. THz pulses are also generated through optical rectification, a nonlinear optical process based on degenerate difference frequency mixing [30]. Both methods require an ultrafast (~ 100 fs) optical laser source to drive the processes.

In the case of photoexcited free carrier transport, the short optical pulse is required to generate a transient current with a rapid rise time, which in turn radiates electromagnetic waves with THz frequencies. In the case of optical rectification, the short pulses are required for the high intensities needed for efficient nonlinear optical interactions to build up the radiated THz field.

Optical rectification is a popular and efficient technique used for the generation of THz radiation, as it only requires a nonlinear optical crystal with a second order nonlinearity to be placed in an intense laser beam. The optical excitation pulse undergoes degenerate difference frequency generation, which induces a DC polarization of the crystal lattice. The nonlinear process depends on the optical excitation intensity, and so the induced DC polarization tracks the intensity profile of the excitation pulse, and the transient polarization then radiates a THz wave [31].

THz generation from a semiconductor-based photoconductive antenna with external bias can be thought of as occurring in several steps. An optical pulse creates carriers in the conduction band of a semiconductor substrate which experience a static bias field. The photo-injected electrons and holes are accelerated in the DC bias field, creating a current transient with a rise time on the order of the optical excitation pulse width. The time-dependent current leads to a radiated THz electric field (Figure 3) according to Maxwell's equations.

In the case of strong illumination, large photo-carrier densities can be produced, and carrier separation by the bias field can lead to an opposing field which screens the applied DC field. This space-charge screening typically limits the output power of photoconductive switches that generate THz radiation. These processes all happen on a sub-picosecond timescale. On a much longer time scale of approximately nanoseconds between laser pulses, the photocarriers either recombine or travel to the electrodes, and the THz emitter system goes back to its initial state, ready to repeat these processes again.

In the experiments conducted in this work, we use photoconductive sources and detectors, and so we will focus on the physics of these types of sources for the remainder of my thesis.

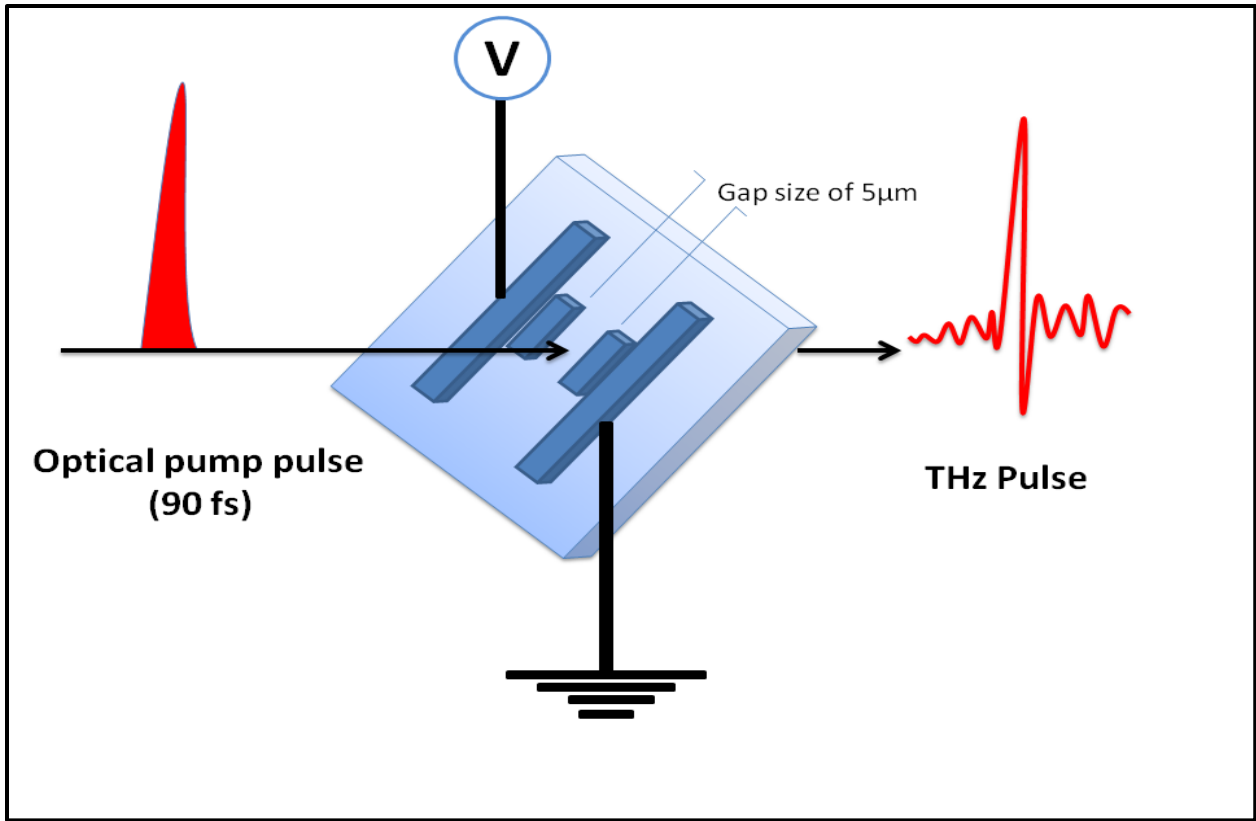


Figure 3. Photoconductive THz emitter.

As described previously, when a fs laser (high-intensity optical pump) excites a biased semiconductor with photon energies greater than its bandgap, electrons and holes are produced in the conduction and valence bands, respectively. The rapid change in photocarrier density within a photoconductive antenna, because of absorption of the fs pump and subsequent acceleration in the applied dc bias field, E_b , produces an electromagnetic field radiating into free-space [32].

The production of ultrashort current transients with a FWHM of 1 ps (or less) requires the carrier lifetime in the semiconductor to be short [32]. Although some semiconductors have a carrier lifetime of hundreds of ps, there are techniques (eg. radiation damage and ion implantation) which allow the carrier lifetime to be significantly reduced to even sub-ps durations. For example, low-temperature grown GaAs (LT-GaAs) has a photocarrier lifetime τ_c of 0.25 ps [32]. Furthermore, the short duration of the pulse in the time domain leads to a broad bandwidth [33].

In a photoconductive THz emitter, when the radiation emerges from the rear surface of the substrate, it is strongly divergent as a result of the dipole nature of the source. The emitted radiation is first collected with a substrate lens to collimate the radiation, followed by conventional far-infrared optics to work with the collimated beam.

The resulting THz beam can be focused as a regular Gaussian laser beam, however, the long-wavelength radiation diffracts more readily than optical beams and limits the ultimate focal spot of the radiation [34]. A well-collimated THz beam of approximately 1 cm radius can propagate for several meters before diffraction becomes appreciable [35].

The detection of the THz field occurs on an identical photoconductive antenna to the emitter, where instead of an external voltage bias, the THz pulse to be detected serves as the bias field for the antenna, which drives the photogenerated carriers in the antenna circuit [35]. THz detection is a difficult task since the power of emitted THz signals is weak [32].

The output signal is dependent on the incident THz field amplitude, the probe power and pulsewidth, and also depends on the physical parameters of the photoconductor itself. The detection process uses the same physical principles as the emitter, replacing the bias field with the THz field itself.

The photocurrent is sampled by varying the delay of the fs gate beam with respect to the THz beam, using an optical delay line. This measured current of photogenerated carriers will be a reliable representation of the actual THz field provided that a fast substrate is used (with a sub-ps carrier recombination time) [35].

The characteristics of the measured THz signals will be described in more detail later in this thesis, however, at this point we introduce the model which we use to predict the THz interaction with NO in the time domain at specific temperature and pressure.

Chapter 3

Rotational spectroscopy model of nitric oxide

This chapter develops the physical model we use to treat the interaction of THz radiation with NO. We extend the theoretical model proposed by Harde and Grischkowsky [36, 42] to include more complicated effects of the unpaired valence electron in NO. Once the model is developed, it is implemented in the Matlab programming environment to simulate the transmitted THz signal through NO based on an experimentally measured reference waveform. The model parameters can be varied and used as fitting parameters, and using experimental data, the fitting error can be minimized to obtain a best-fit curve and subsequent measurement of the molecular parameters of NO.

3.1 Model for NO

We now develop the model for the interaction between THz radiation and NO molecules at a specific temperature and pressure. In order for this model to be suitable for comparing to experimental measurements, it is necessary to model the time-domain response of a THz pulse propagating through a gas of NO molecules at a specific temperature and pressure.

First, we need to understand the electronic configuration of the NO-Molecule as shown, for example, in figure 4 below.

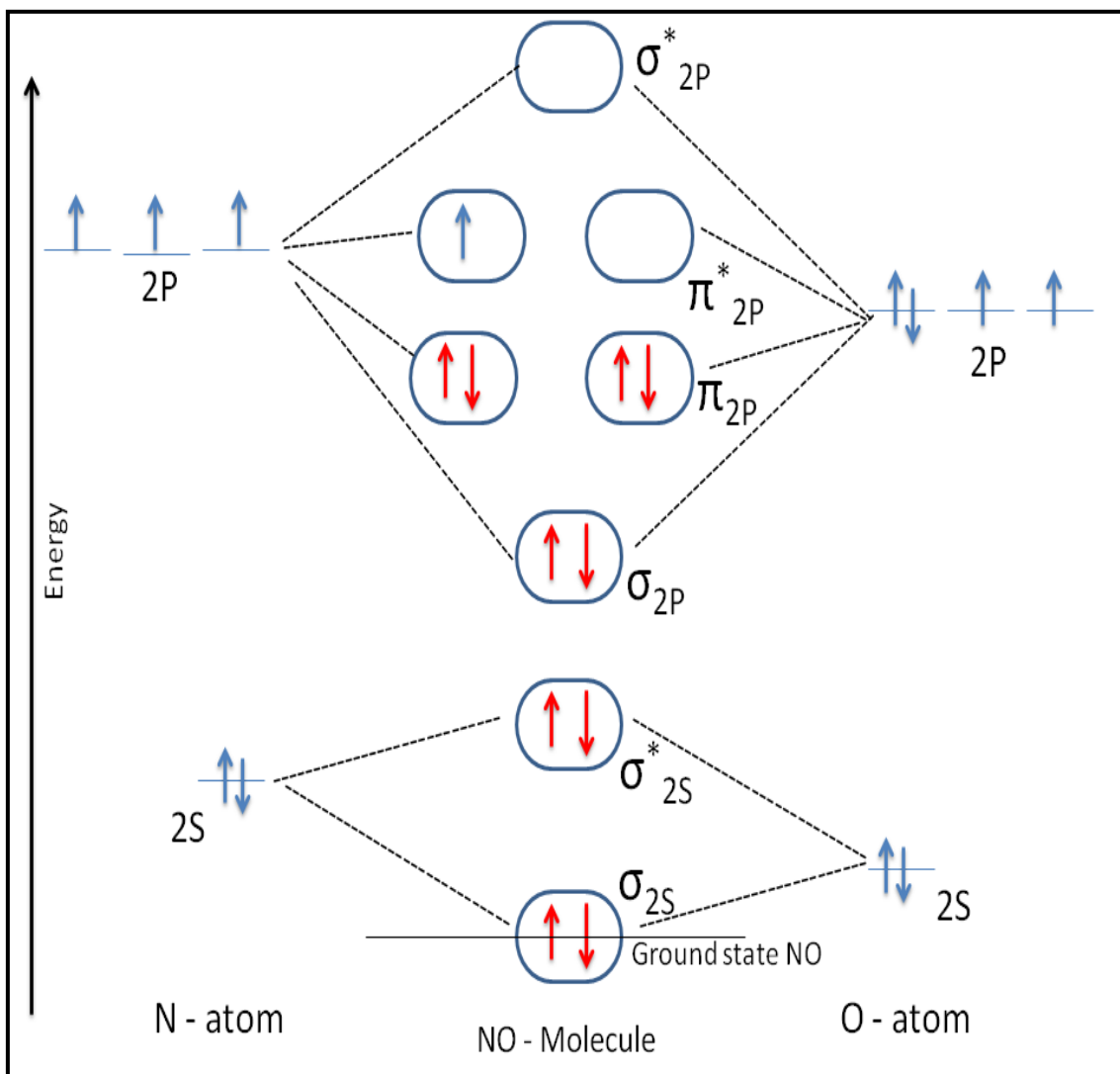


Figure 4: Molecular orbital diagram of NO in the electronic ground state.

As shown in Figure 4, the 2S and 2P atomic molecular orbitals of oxygen are slightly lower in energy than those of nitrogen, as a result of the larger electronegativity of oxygen in comparison to nitrogen.

The lower-energy molecular orbitals of NO, such as : σ_s , σ_p , π_s and π_p are called *the bonding molecular orbitals*, and the higher energy molecular orbitals, such as σ_s^* , σ_p^* , π_s^* and π_p^* are called *the anti-bonding molecular orbitals* (which are labeled by an asterisk) [37], where the anti-bonding orbital weakens the bond between two atoms, and the electrons in the anti-bonding orbitals are easily released from the atom. The electron in the lower-energy bonding molecular orbital is more stable than the electron in the higher-energy anti-bonding molecular orbital. As a result, the lower-energy orbitals in NO are filled with the 10 valence electrons, leaving one unpaired electron located in the higher-energy orbital π_{2p}^* .

The unpaired electron of NO is in a ${}^2\Pi$ -state, with an angular momentum quantum number $l = 1$. Thus, the total angular momentum has contributions from the spin angular momentum and the orbital angular momentum ($J = S + 1$), and has a value of either 1/2 or 3/2 due to spin-orbit coupling. This leads to the two different ${}^2\Pi$ -states observed in a sample of NO: ${}^2\Pi_{1/2}$ and ${}^2\Pi_{3/2}$. The fraction of NO molecules that are in the ${}^2\Pi_{1/2}$ state, which represented by $f_{2\Pi_{1/2}}$, and the fraction of NO molecules that are in the ${}^2\Pi_{3/2}$ state, which represented by $f_{2\Pi_{3/2}}$, sum to give the total fraction f_0 of the NO molecules in the lowest vibrational state:

$$f_0 = f_{2\Pi_{1/2}} + f_{2\Pi_{3/2}} \quad , \quad (1)$$

where $f_0 \approx 1$ at room temperature ($\cong 20$ °C) because of the relatively large separation of vibrational states ($\cong 1904$ cm^{-1}) compared to k_bT ($\cong 203$ cm^{-1}).

This molecular response theory must be applied separately for the two different electronic states of NO as they have different rotational energies (resulting from the different rotational constants associated with the different geometries). Therefore, the fractions of molecules in each state must be known, and can be obtained if we assume the NO gas is in equilibrium using Boltzmann statistics [38].

$$N_{2\Pi_{1/2}} = Ae^{\frac{-E_{2\Pi_{1/2}}}{k_B T}}, \text{ and } N_{2\Pi_{3/2}} = Ae^{\frac{-E_{2\Pi_{3/2}}}{k_B T}}, \quad (2)$$

where we can determine the fraction of molecules in each state using the ratio:

$$\frac{N_{2\Pi_{3/2}}}{N_{2\Pi_{1/2}}} = \frac{f_{2\Pi_{3/2}}}{f_{2\Pi_{1/2}}} = e^{\frac{-(E_{2\Pi_{3/2}} - E_{2\Pi_{1/2}})}{k_B T}}, \quad (3)$$

where A is a normalization constant, f is the fraction of molecules in each state (the sum of these two fractions add to one), E is the energy of the individual states, k_B is Boltzmann's constant, and T is the temperature of the gas in Kelvin.

Following the work of Harde, the molecules in each electronic state are assumed to have a van Vleck-Weisskopf line-shape for their rotational transitions [36]. The interaction of the electric field with the sample in the frequency domain is calculated by modeling the absorption $\alpha(\omega)$ and the dispersion $\Delta\kappa(\omega)$, using the van Vleck-Weisskopf line-shape function for the absorption and dispersion [39].

For higher frequencies of optical and infrared transitions, the simple Lorentzian line-shape [40] provides excellent agreement with experiment, particularly for the central region of absorption lines [41]. Lower frequencies (in the range of microwave or far-infrared, and under conditions when a linewidth becomes comparable to the transition frequency), the absorption profile of a collisionally broadened line is better represented by the van Vleck–Weisskopf line-shape [41].

Our measurements are well-fit using a van Vleck-Weisskopf line-shape for an individual transition frequency of order ~ 1 THz. The difference between the Lorentz and van Vleck–Weisskopf theory is that the response of a molecule to an external field is considered in its two limiting cases [41]. The Lorentz line-shape assumes that after a collision, molecules are oriented randomly with respect to the driving field, and therefore no macroscopic polarization in the sample will be found. van Vleck-Weisskopf line-shapes take into account Boltzmann statistics, assuming instantaneous realignment during a collision such that the molecules are oriented as to have a low energy in the field [41].

The propagation of a plane wave with electric field profile $E(z, t)$, which propagates in the z -direction, can be calculated from its frequency spectrum, absorption, and dispersion as [36] :

$$E(z, t) = \int_{-\infty}^{\infty} E(\omega) \exp[-i(\omega t - \kappa_0 z)] \exp\left[\left(i\Delta\kappa(\omega) - \frac{1}{2} \alpha(\omega)\right) z\right] d\omega, \quad (4)$$

where $E(\omega)$ is the spectral field distribution, which can be found from the Fourier transform of the initial THz pulse, which is given by [42]:

$$E(\omega) = \frac{1}{2\pi} \int_{-\infty}^{\infty} E(0, t) \exp(i\omega t) dt , \quad (5)$$

where $E(0, t)$ represents the time varying electric field obtained in the absence of a gas sample (the reference waveform), t is time, ω is the angular frequency, z is the gas cell path length, and the phase change per unit length introduced by an index of refraction, n , of the sample is given by:

$$\kappa_0 = \omega n / c , \quad (6)$$

where κ_0 is the nonresonant wave vector in the sample and c is the speed of light in vacuum.

The electric field can be expressed in the time domain by the inverse Fourier transform:

$$E(z, t) = \int_{-\infty}^{\infty} E(\omega) \exp\{-i [\omega t - \kappa(\omega)z]\} d\omega , \quad (7)$$

where we can describe the interaction of the electric field with the NO-gas in the frequency domain by introducing the linear polarizations as [42]:

$$P(\omega) = \varepsilon_0 \chi(\omega) E(\omega) , \quad (8)$$

where ε_0 is the vacuum permittivity, $\chi(\omega)$ is the complex electric susceptibility and we have $E(\omega)$ from equation (5), giving:

$$P(z, t) = \varepsilon_0 \int_{-\infty}^{\infty} \chi(\omega) E(\omega) \exp\{-i [\omega t - \kappa(\omega)z]\} d\omega , \quad (9)$$

where $\kappa(\omega)$ is given by:

$$\kappa(\omega) = \kappa_0 \left[1 + \frac{\chi(\omega)}{n^2} \right]^{1/2} \cong \kappa_0 \left[1 + \frac{1}{2n^2} \chi'(\omega) + \frac{i}{2n^2} \chi''(\omega) \right], \quad (10)$$

From linear dispersion theory, the real part of $\chi(\omega)$ changes the phase per unit length from κ_0 to $\kappa_0 + \Delta\kappa$, with

$$\Delta\kappa(\omega) = (\kappa_0/2n^2)\chi'(\omega), \quad (11)$$

and the imaginary part causes the amplitude to be exponentially attenuated with distance, z , according to $\exp(-\alpha z/2)$, so the power absorption coefficient is given by:

$$\alpha(\omega) = (\kappa_0/n^2)\chi''(\omega), \quad (12)$$

where $\alpha(\omega)$ is the absorption. By knowing $\chi(\omega)$, we can find $\kappa(\omega)$ from Equation (10) and by using this new value of $\kappa(\omega)$ in Equation (4), we know the propagation of the pulse $E(z, t)$ through the gas cell.

Finally, by using Equation (11) and Equation (12) we can get a new form for $\kappa(\omega)$, which can be used in Equation (7) resulting in our final pulse propagation form, $E(z, t)$, as written in Equation (4). In the case of randomly oriented molecules, the absorption coefficient α_J corresponding to a single rotational transition $J \rightarrow J+1$ of a sample of linear molecules of NO can be written as [42]:

$$\alpha_J(\omega) = \frac{p f_0 \mu^2 h B_v \omega^2}{6 n c \varepsilon_0 (kT)^3} (J + 1) e^{\frac{-hB_v J(J+1)}{kT}} G_A(\omega, \omega_J) , \quad (13)$$

where, p is the sample pressure, μ is the electric dipole moment of NO, B_v is the rotational constant for vibrational state v , h is Plank's constant, n is the index of refraction of the NO gas, c is the speed of light in vacuum, ε_0 is the permittivity of free space, k_B is Boltzmann's constant, $k_B T$ is the thermal energy, ω_J is the angular frequency associated with the $J \rightarrow J+1$ rotational transition, and $G_A(\omega, \omega_J)$ is the van Vleck-Weisskopf absorption line-shape function which is given by [36]:

$$G_A(\omega, \omega_J) = \frac{\Delta\omega_J}{(\omega - \omega_J)^2 + (\Delta\omega_J/2)^2} + \frac{\Delta\omega_J}{(\omega + \omega_J)^2 + (\Delta\omega_J/2)^2} , \quad (14)$$

where $\Delta\omega_J$ is the angular frequency linewidth (FWHM) of the absorption line of the $J \rightarrow J+1$ rotational transition. The transition frequencies are determined by:

$$\frac{\omega_J}{2\pi} = 2 B_v (J + 1) - 4 D_v (J + 1)^3 , \quad (15)$$

where B_v is the rotational constant of the vibrational state which is related to the moment of inertia $I = \mu R^2$; (μ is the reduced mass " $\mu = M_A M_B / (M_A + M_B)$ ", and R is the bond length) of the molecule.

A diatomic molecule with the atomic masses M_A and M_B can rotate around any axis through the center of mass as shown in figure 5.

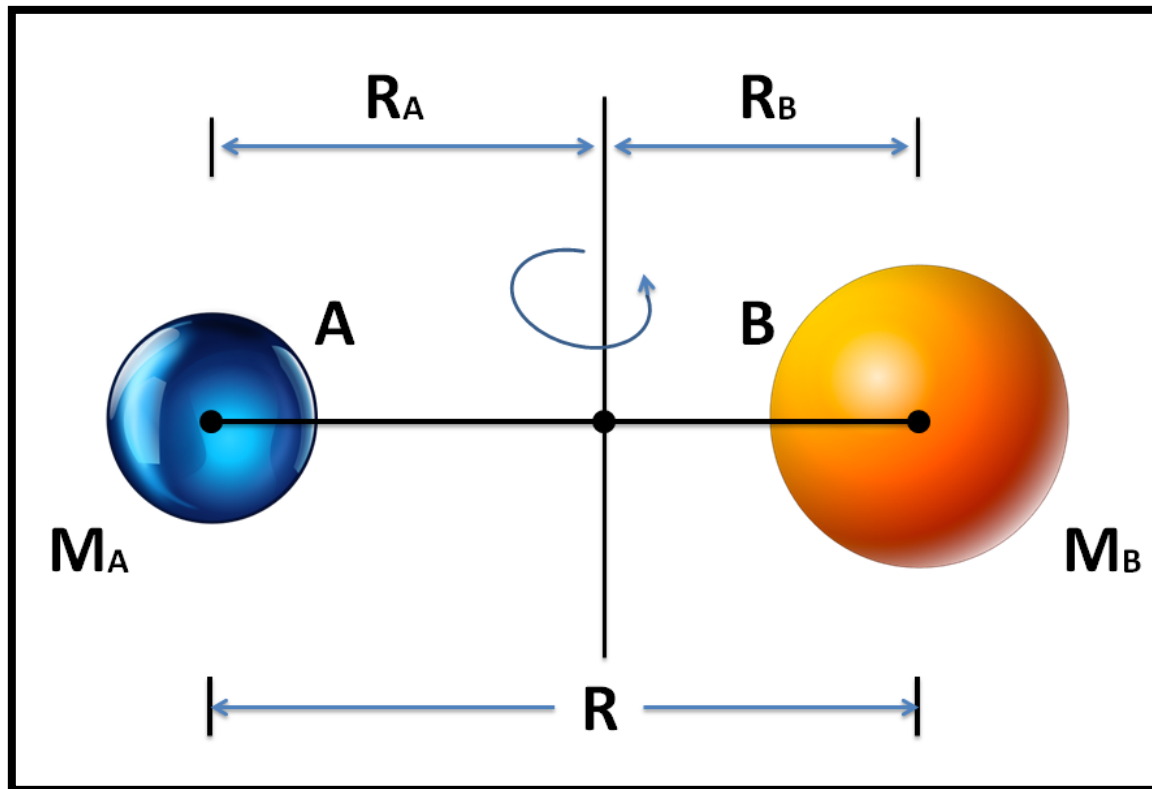


Figure 5. Diatomic molecule as a rigid rotor. M is the mass and R is the distance from the center of masses.

The rotational constant, B_v , of the ground vibrational state ($v=0$) can be determined by:

$$B = \frac{h}{8 \pi^2 c I_B} \quad , \quad (16)$$

and D_v in Equation (15), is the centrifugal stretching constant of the ground vibrational state ($v=0$).

In some cases, if a chemical bond is weak enough so that the nuclei respond to increasing rotational energy by moving farther apart, the molecule experiences centrifugal elongation. In other words, D_v is related to the increase in bond length with increasing rotational energy.

For the change of the wave vector, the corresponding dispersion response for the $J \rightarrow J+1$ rotational transition is given by [42]:

$$\Delta K_J = \frac{P f_0 \mu^2 h B_v \omega \omega_J^2}{3 n c \epsilon_0 (kT)^3 (\omega_J^2 - \omega^2)} (J + 1) \exp\left[\frac{-h B_v J(J+1)}{kT}\right] G_N(\omega, \omega_J), \quad (17)$$

where $G_N(\omega, \omega_J)$ is the van Vleck-Weisskopf dispersion line-shape function given by [42]:

$$G_N(\omega, \omega_J) = 1 - \frac{\omega \Delta\omega_J^2}{8 \omega_J^2} \left[\frac{\omega + \omega_J}{(\omega - \omega_J)^2 + (\Delta\omega_J/2)^2} + \frac{\omega - \omega_J}{(\omega + \omega_J)^2 + (\Delta\omega_J/2)^2} \right], \quad (18)$$

The absorption and the dispersion over the whole spectral range of the terahertz pulse is found summing equations (13) and (17) over all transitions within the bandwidth of our THz pulses.

The absorption and dispersion of the THz pulse can then be obtained by adding the corresponding values for all of the transitions that lie within the spectral bandwidth of our system. So the total dispersion $\Delta k(\omega)$ and absorption $\alpha(\omega)$ can be found by taking the sum of equation (7) of $\alpha_j(\omega)$ and taking the sum of equation (11) of Δk_j within the spectral range of the incident THz pulse for all the rotational transitions.

In principle, we can include all transitions. In practice, there are both a limited number of thermally populated rotational energies at room temperature, and a finite number of transitions that fall within the bandwidth of the THz pulses. In applying the model, we therefore restrict our attention to the lowest 100 transitions in NO, which we find to be more than sufficient to capture the important transitions. Thus, the total absorption and the total dispersion are found by using the following equations:

$$\alpha(\omega) = \sum_{J=0}^{J=100} \alpha_J(\omega) \quad (19)$$

$$\Delta k(\omega) = \sum_{J=0}^{J=100} \Delta K_J \quad (20)$$

This model can then be used to predict the shape and amplitude of the THz commensurate echoes seen in the time domain when THz radiation is passed through a gas sample of NO. In this case, there are three variable parameters for the model:

- 1- The rotational constant of the ground vibrational states (${}^2\Pi_{1/2}$ and ${}^2\Pi_{3/2}$), $B_0^{1/2}$ and $B_0^{3/2}$,
- 2- The centrifugal stretching constant for the ground vibrational states (${}^2\Pi_{1/2}$ and ${}^2\Pi_{3/2}$), $D_0^{1/2}$ and $D_0^{3/2}$, and
- 3- The collisional time constant, τ_c , which dictates the linewidth (i.e. dictates the angular frequency linewidth $\Delta\omega$, which is the variable parameter in the model; $\tau_c = 1/\Delta\omega_J$).

All of the other parameters are either physical constants, or values taken from the literature as we will describe in the next chapter, where we will describe our experimental work, so that we can compare this theoretical model with our experimental data.

Chapter 4

Experimental setup and results

4.1 Experimental setup

The model described in Chapter 3 will be used to analyze experimental data collected and to determine the limits of detection for NO sensing using THz-TDS. We use the THz Menlo-system GmbH, (Model: TC-1550), available in our lab at UNBC, which generates THz pulses using photoconductive switches excited with a frequency doubled, 90 fs, 1550 nm fiber laser. As described in section 2.4, the fs laser generates carriers in the conduction band of the photoconductive emitter which are accelerated in the DC bias field creating a time dependent current transient, radiating the THz electric field.

The THz field is collimated with a substrate lens, followed by conventional far-infrared optics to guide the THz beam through a gas cell which can be placed under vacuum or filled with a variable pressure of NO. The transmitted THz beam is collected and focused onto a photoconductive detector, and by varying the delay of the laser gate beam on the

photoconductive detector with respect to the THz beam, the transmitted THz field can be mapped out in time.

The experimental set-up is shown in Figure 6 below. The NO gas is contained within a gas-cell which has a length of 13.64 cm. This cell has high resistivity silicon windows, and is used at pressures below 1 atm to avoid leakage. At room temperature ($T = 293$ K), different partial pressures of NO are introduced, and can be mixed with N_2 to bring the total pressure up to a constant value of approximately 1 atm.

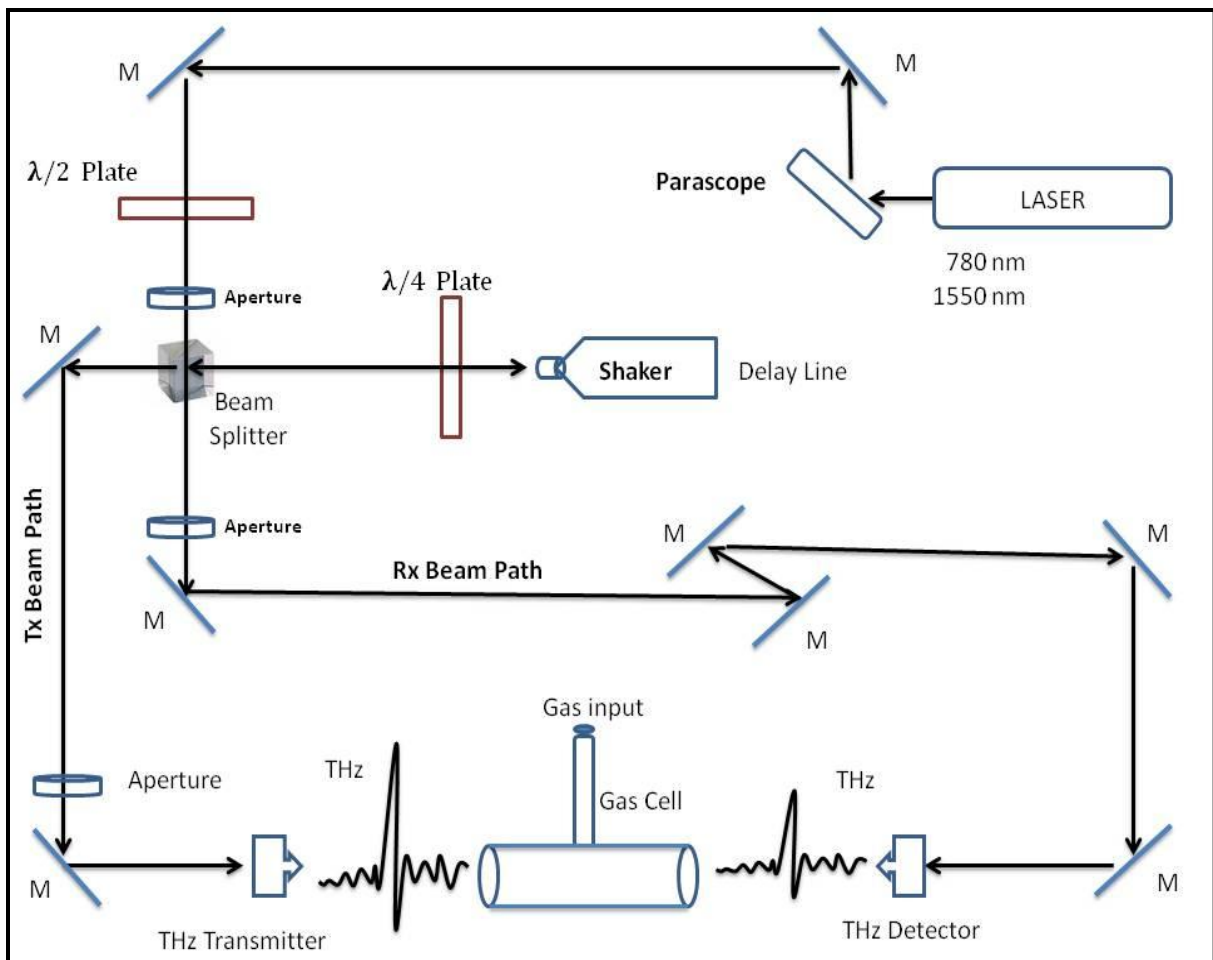


Figure 6. Menlo system setup.

The pulses from the femtosecond-laser are split into two different beams, where the first beam is *the pump beam (Tx)*, which excites the photoconductive emitter, and the second one is *the probe beam (Rx)*, which samples the THz field in the photoconductive detector.

The pump pulses are focused onto the THz emitter using a microscope objective to illuminate the 5 μm gap of the emitter. The other beam passes through the delay stage, which introduces a variable delay between the pump beam and the probe beam before the probe is focused by a microscope objective onto a photoconductive detector that matches the emitter. By varying the delay of the probe relative to the pump, the THz field can be sampled at different points in time, and the full temporal profile of the THz field can be collected.

A stainless steel gas cell with high-resistivity silicon windows was used to introduce NO for investigation. The gas cell is connected to a NO-gas cylinder and to a N₂-gas cylinder, as well as a vacuum pump, which allows us to take a reference scan under vacuum conditions. In addition, a secondary N₂-gas source is connected to our THz spectroscopy system, where it is used to purge the whole system to avoid absorption of the THz beam by atmospheric water vapour.

The Menlo system setup (Figure 6) can be used to perform THz spectroscopy in the time domain, where the detection is coherent. A Fast Fourier Transformation (FFT) of our experimental data can be performed, which allows us to also study the THz pulse in the frequency domain.

An example of a THz pulse (in the time and frequency domains) is shown in figure 7 .

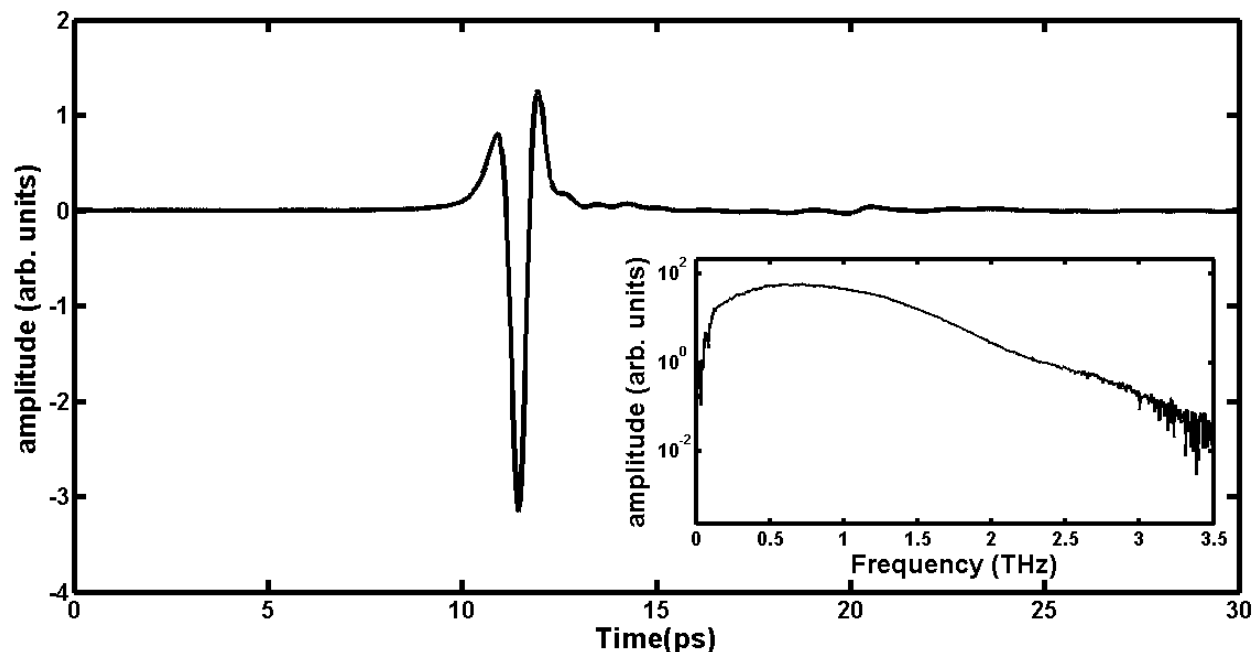


Figure 7. Example of THz waveform in the time domain passing through a 13.64 cm gas-cell under vacuum. The inset shows the THz field in the frequency domain obtained through FFT.

The coherent detection obtained using the photoconductive antennas is demonstrated in Figure 7, where the electric field of the THz pulse is measured directly as a function of time. This electric field transient is measured on a sub-ps timescale, and both amplitude and phase information is obtained at the same time. The short (sub-ps) duration of the pulse leads to a broad frequency spectrum (shown in the inset of Figure 7) that extends up to about 3 THz.

When we talk about terahertz time-domain spectroscopy (THz-TDS), we are referring to transmission spectroscopy using the THz field profile like the one shown in figure 7, and studying the effect of introducing NO on the field profile in time (main figure), rather than what is traditionally done, which is to study the response in the frequency domain (inset of figure 7).

The power of time domain measurements can be seen by looking at the interaction between the THz and NO molecules, which leads to commensurate echoes as shown in figure 8.

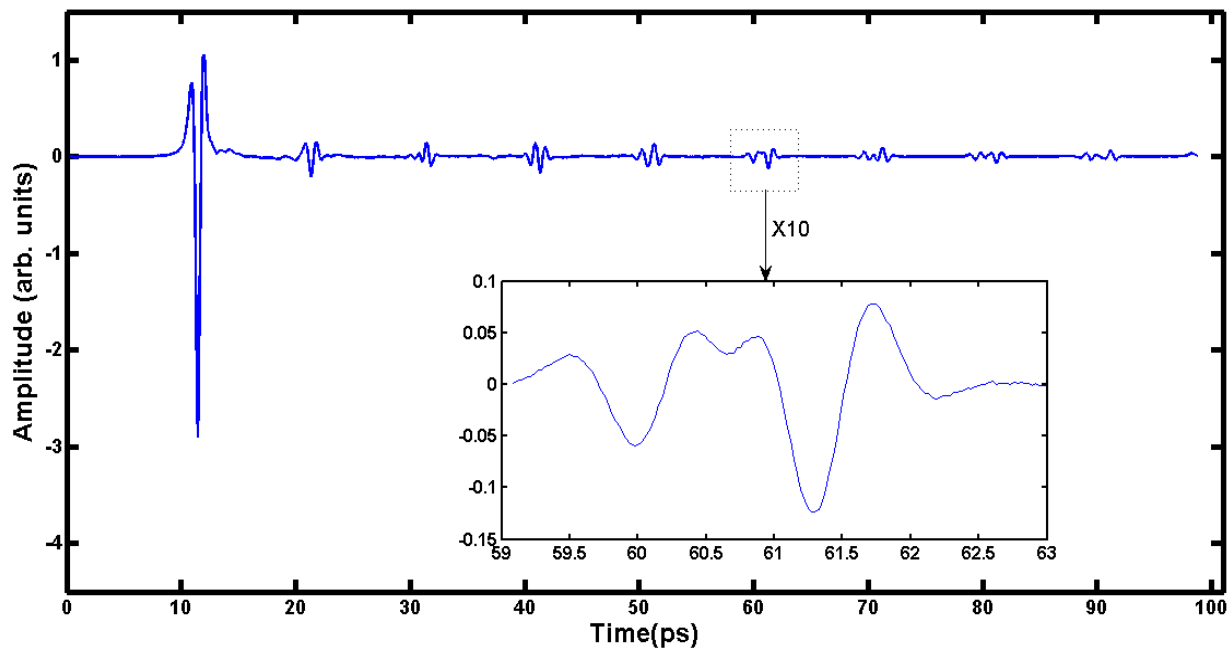


Figure 8. Example for the time domain response for NO at partial pressure $p = 750$ mmHg (with added N_2 to the gas-cell to reach total pressure of 1 atm). The periodic echoes are referred to as “THz commensurate echoes.”

Fourier transformation to the frequency domain reveals the periodically spaced absorption lines that are traditionally associated with spectroscopy and is shown in Figure 9 below.

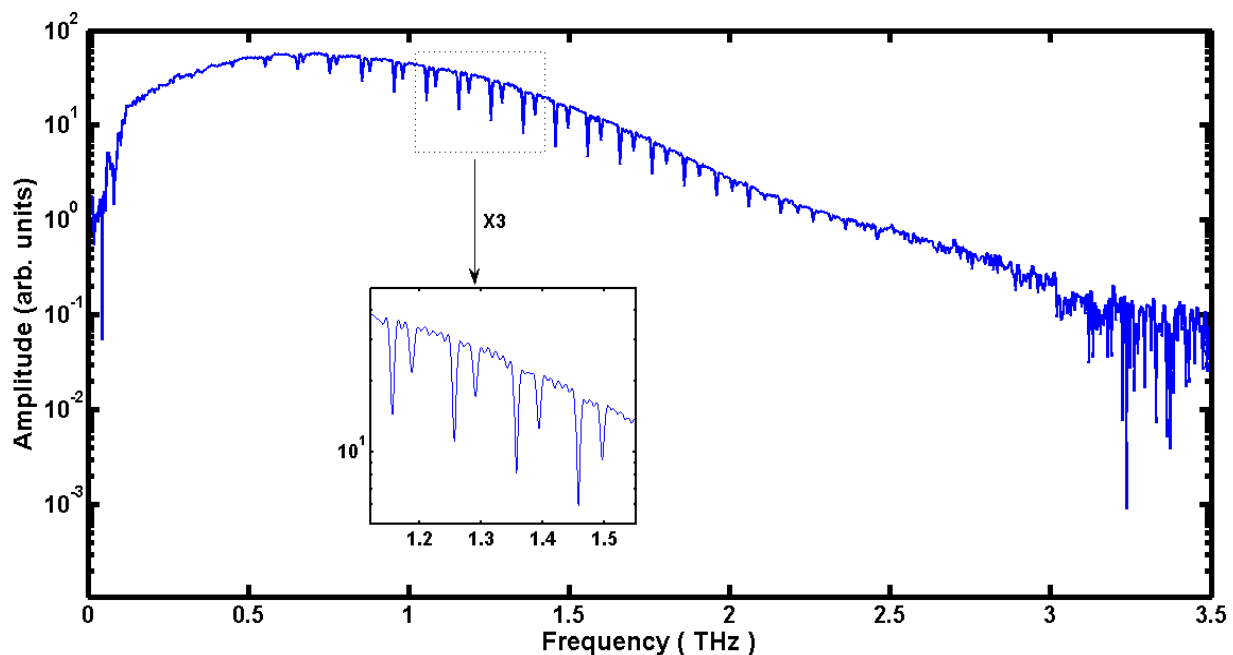


Figure 9. The frequency domain response for NO at partial pressure $p = 750$ mmHg. The inset shows the closely spaced absorption lines present from the two electronic states in NO.

The time domain echo profiles contain information about molecular structure similar to what we traditionally gather from the frequency domain (i.e. the fingerprint of the absorption lines which is used to study gas spectroscopy).

In the frequency domain (figure 9), the two different states (${}^2\Pi_{1/2}$ and ${}^2\Pi_{3/2}$) are clearly observable as each exhibits their own manifold of absorption lines which are closely spaced, but of different amplitude. In the time domain, the different states manifest as separate pulses (noticeably more separated at longer times in Figure 8).

The difference in amplitude results from the Boltzmann distribution which dictates the thermal population fraction in each of the two electronic states. As shown before in section 3.1, the absorption coefficient α_J of a sample of NO can be written as:

$$\alpha_J(\omega) = \frac{p f_0 \mu^2 h B_v \omega^2}{6 n c \epsilon_0 (kT)^3} (J + 1) e^{\frac{-hB_v J(J+1)}{kT}} G_A(\omega, \omega_J) , \quad (13)$$

Where the experimental absorption of NO is obtained by using Lambert-Beer's law, which is a relationship between absorbance and concentration of an absorber of electromagnetic radiation, which is given by:

$$I = I_0 e^{-\alpha z} , \quad (21)$$

where I_0 and I are the initial and final intensity of electromagnetic radiation passing through a sample of distance equal to z , which gives the absorption coefficient, α , as a function of the electric field, E , as:

$$\alpha = \frac{-2}{z} \ln \left(\frac{E}{E_0} \right) \quad (22)$$

The model waveform and the experimental absorption for NO calculated from Figure 9, are shown in figure 10.

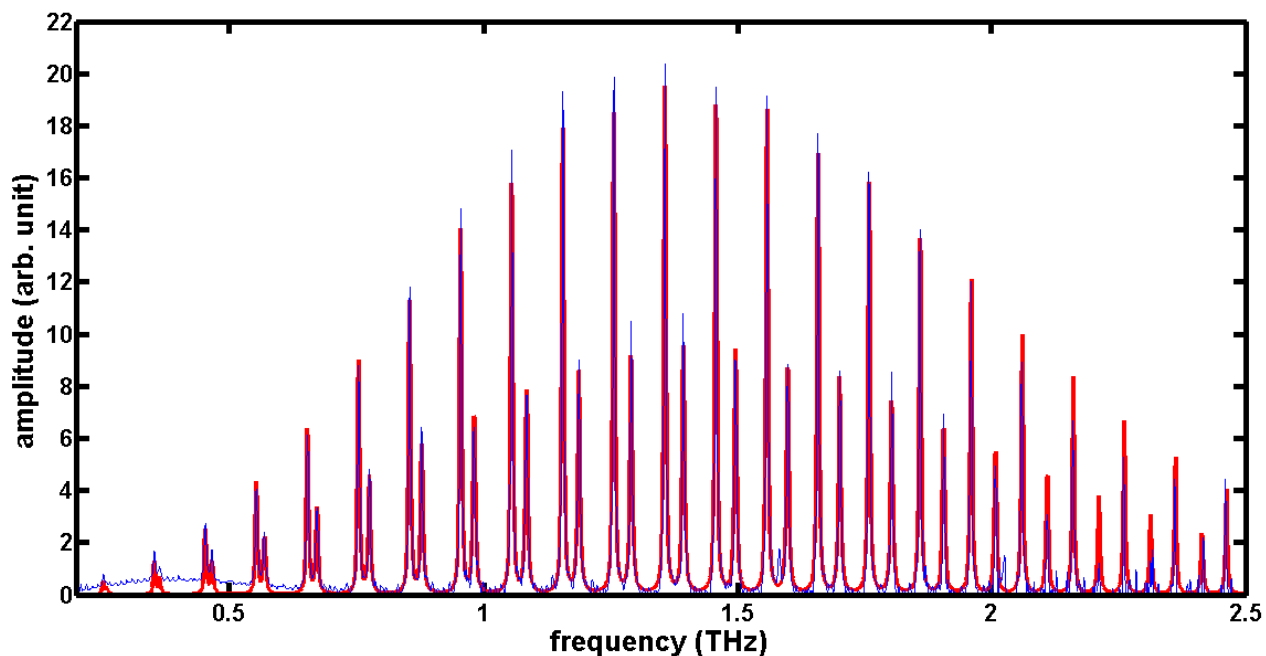


Figure 10. Absorbance spectrum of NO at partial pressure $p = 750$ mmHg (with total pressure of 1 atm), showing both electronic states ${}^2\Pi_{1/2}$ and ${}^2\Pi_{3/2}$ which appear as two interlaced manifolds of rotational absorption lines (with two different amplitudes). Model waveform is shown in red, and data waveform shown in blue.

Notice that the theoretical and experimentally measured absorption spectrum in figure 10 agree very well, including the relative amplitude of the two rotational manifolds, and the distribution in frequency. The values used for the three variable model parameters are the best-fit values that are described in the next sections.

The next part of this thesis will be to use the theoretical model that describes the time and frequency domain responses, and to compare to experimental measurements. Then, we will use this comparison in order to fit and obtain best-fit values of the physical parameters, which gives us the minimum difference between the experimental data and the theoretical model.

4.2 Fitting the data to the model

In the previous section, we showed that the model does indeed predict the nature of the transmitted THz pulse in the frequency domain (absorbance spectrum in figure 10). In order to obtain the theoretical fit to the transmitted data in the time domain, it is necessary to find the best values for the fitting parameters. In this section of my thesis, we will discuss how the physical parameters are extracted from the measured transmission data using the model we have developed by using fitting values which minimize the difference between the theoretical model and our experimental data.

The minimization is carried out using the Matlab programming environment to find the best fit values which minimize the sum of squared error (SSE) between the fitting model and the data. We will show some examples of extracting the best fit value. The value that minimizes the SSE is selected, where all of the best-fit values are extracted in the same way.

We iteratively fit the values of n , B_0 , D_0 and τ_c until we achieve convergence, where the values no longer appreciably change. For example, first, we obtain the best fit value of n , by keeping the other physical parameters constant. Then we obtain the best-fit value for B_0 by keeping the remaining values constant and using the best-fit value of n . The best fit value of τ_c is then calculated using the best fit values of n and B_0 . This process is then iterated using these best-fit values, and the procedure is repeated until n , B_0 , D_0 and τ_c do not change appreciably. The values can then be compared to the values from the literature.

4.2.1 Fitting for the refractive index n

The difference in the refractive index, Δn , (taking $n = 1 + \Delta n$) changes depending on the pressure and gas-mix ratio in the gas cell. As we use higher pressures, we get a larger value of the refractive index. This change in n introduces a time-shift between the reference and data scans. The index of refraction is therefore left as a free parameter in the model, allowing us to fit the transmitted signal appropriately in time.

The fitting of the refractive index allows us to get a minimum time-domain shift between our experimental data and the theoretical model. This effectively aligns the two waveforms over the commensurate echoes as shown in figure 11. *As an example*, if we have a difference in the refractive index equal to $\Delta n = 0.0004$, we will get a notable shift of the model waveform as shown in figure 11. The best-fit value for Δn is found by minimizing the sum of the squared difference (SSE) in the same manner as shown for the rotational constant in the next section.

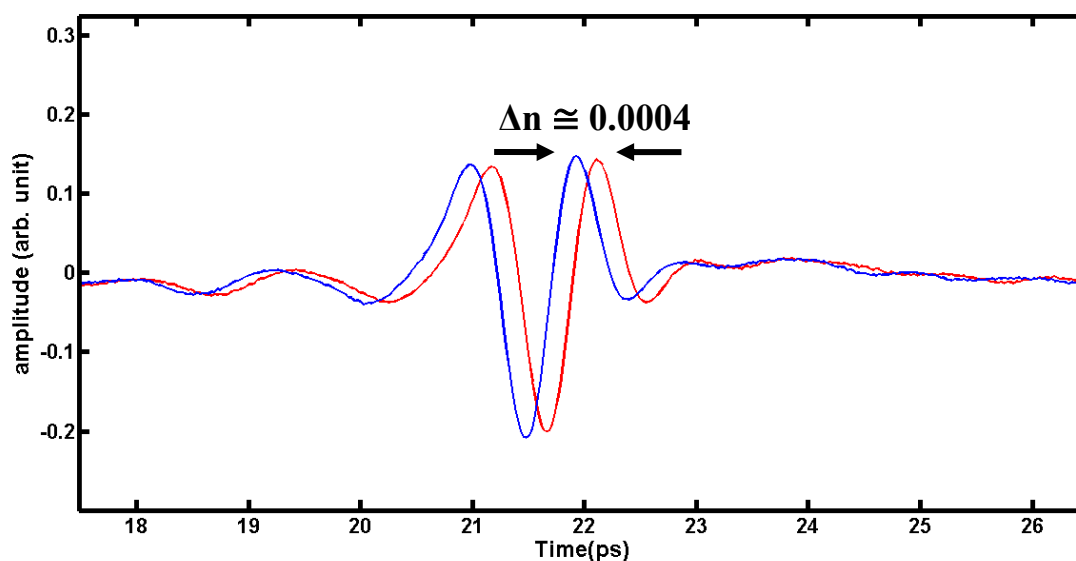


Figure 11. Fitting of the refractive index n of NO at partial pressure $p = 750$ mmHg (with total pressure of 1 atm). Model waveform is shown in red, and data waveform shown in blue.

4.2.2 Fitting of the rotational constant B_0

The best-fit values of the rotational constant for the ground vibrational states (${}^2\Pi_{1/2}$ and ${}^2\Pi_{3/2}$), $B_0^{1/2}$ and $B_0^{3/2}$ are obtained by computing the SSE for each assumed value, and then selecting the value that gives a minimum SSE as shown in Figure 12 for $B_0^{1/2}$.

Where the fitting of $B_0^{1/2}$ and $B_0^{3/2}$ is carried out by using a fixed value of the centrifugal stretching constant of the ground vibrational state (${}^2\Pi_{1/2}$ and ${}^2\Pi_{3/2}$), $D_0^{1/2}$ and $D_0^{3/2}$, which is obtained by finding the best fit values of $D_0^{1/2}$ and $D_0^{3/2}$ while having a pure NO inside our gas-cell (1 atm) as described in section 4.4.

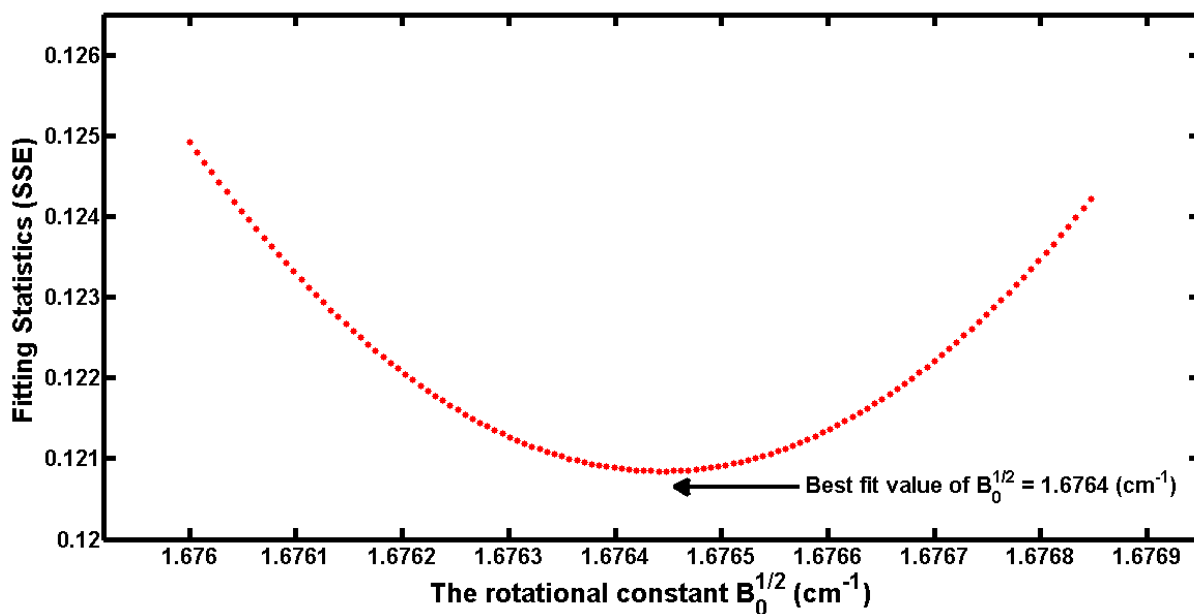


Figure 12. Fitting statistics of the model waveform of rotational constant for the ground vibrational state $B_0^{1/2}$ at $p = 760$ mmHg to obtain best fit value for $B_0^{1/2}$.

In the same way, we can find the best fit value of $B_0^{3/2}$ as shown is in figure 13

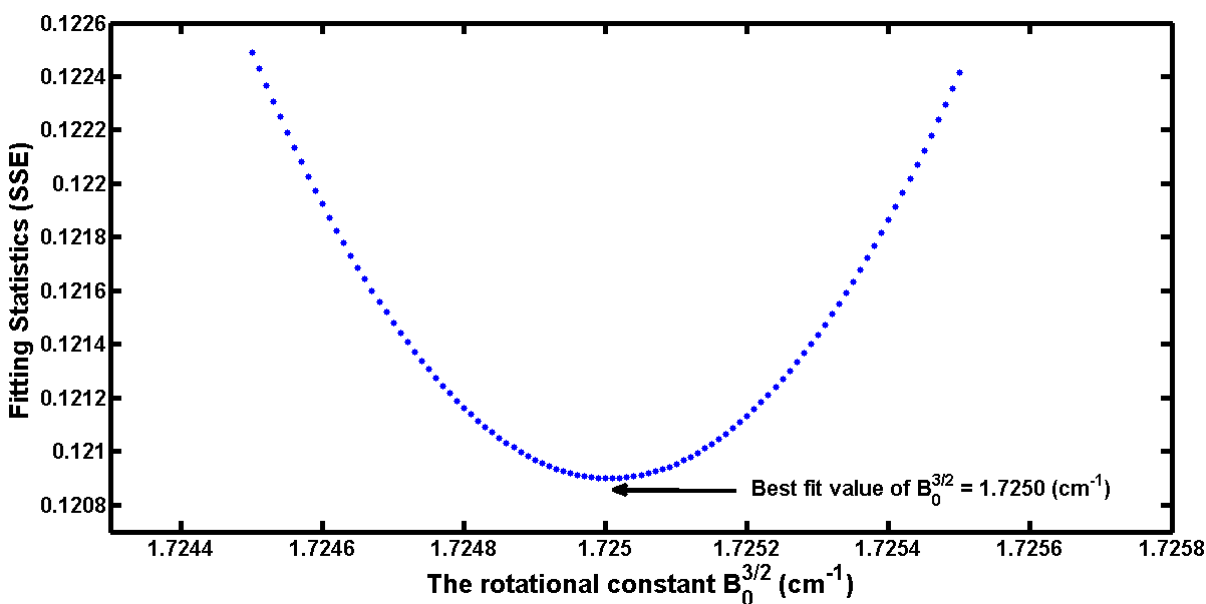


Figure 13. Fitting statistics of the model waveform of rotational constant for the ground vibrational state $B_0^{3/2}$ for NO at $p = 760$ mmHg to obtain best fit value for $B_0^{3/2}$.

As we see in figure 12 and figure 13, it is possible to determine a minimum difference between our theoretical model and the experimental data, which we take as the best fit for the parameter of interest. This best-fit value can be compared to literature values, where some of the published literature values of the rotational constant of the ground vibrational state (${}^2\Pi_{1/2}$ and ${}^2\Pi_{3/2}$), $B_0^{1/2}$ and $B_0^{3/2}$ are listed in table 3 below:

Table 3. Some examples of the published values of $B_0^{1/2}$ and $B_0^{3/2}$ in literature.

published literature values of $B_0^{1/2}$ cm^{-1}	published literature values of $B_0^{3/2}$ cm^{-1}
1.64471 [43]	1.70509 [43]
1.66300 [44]	1.71100 [44]
1.67185 [45]	1.720178 [45]
1.68860 [46]	1.98000 [46]
1.69606 [47]	1.98600 [47]

These published literature values can be compared to the values which we have measured by using THz-TDS. Our results discussed later yield values of $B_0^{1/2} = 1.6763 \pm 0.00058 \text{ cm}^{-1}$, and $B_0^{3/2} = 1.7248 \pm 0.0012 \text{ cm}^{-1}$, which are in the range of the published values.

4.2.3 Fitting of the time constant τ_c

In the same way we calculated a best fit value for the rotational constant, we can find a best fit value of the time constant τ_c . This is done by fitting $\Delta\omega_J$, the angular frequency linewidth FWHM, as in Equation 14, where $\tau_c = \frac{1}{\Delta\omega_J}$:

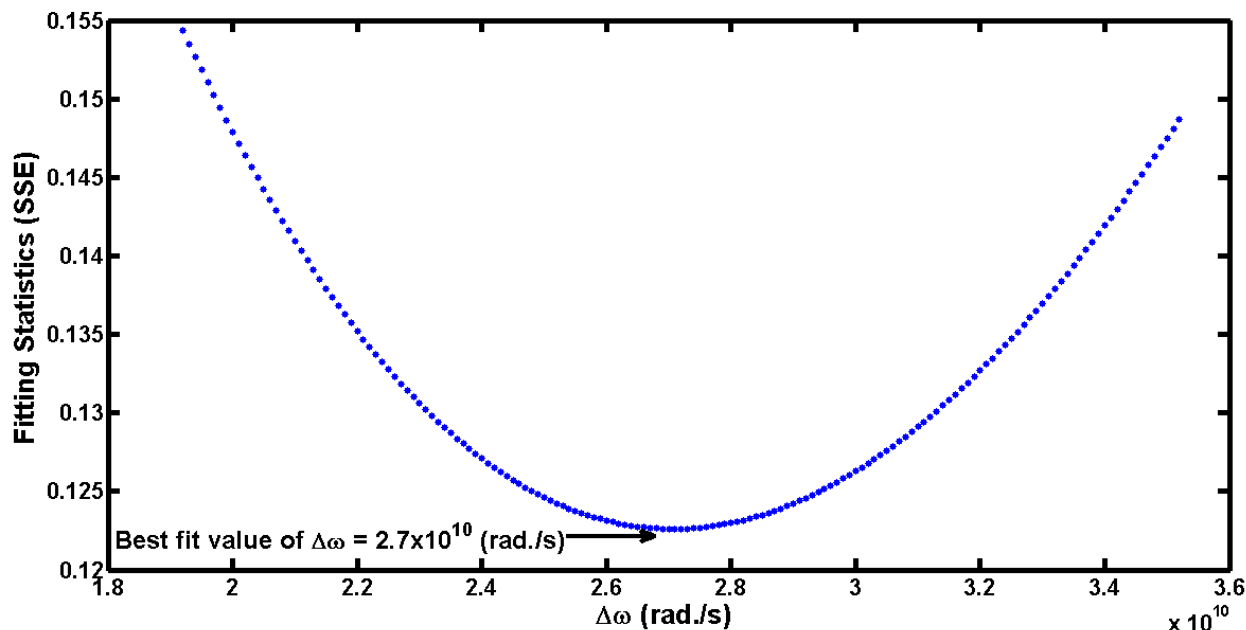


Figure 14. Fitting statistics of the model waveform for the angular frequency linewidth $\Delta\omega_J$ for NO at $p = 760$ mmHg

For this particular pressure ($p = 760$ mmHg), the best fit value of $\Delta\omega_J = 2.7 \times 10^{10}$ rad/sec as shown in figure 14 corresponds to a collisional time constant of:

$$\tau_c = \frac{1}{\Delta\omega_J} = \frac{1}{2.7 \times 10^{10} \text{ rad./s}} = 0.37 \text{ ps}$$

The measured values of the angular frequency linewidth, $\Delta\omega_J$, will be compared to the values published in the HITRAN database later in the results section (shown in figure 24, and 25).

4.2.4 Statistical error estimation and analysis

The error associated with the measurement of the rotational constant of the ground vibrational state (${}^2\Pi_{1/2}$ and ${}^2\Pi_{3/2}$), $B_0^{1/2}$ and $B_0^{3/2}$, or with any of the other parameters obtained by fitting procedure used in this thesis, can be estimated by considering the effect of random noise present in the measured and computed signals.

For the case of the rotational constants of the ground vibrational state $B_0^{1/2}$ and $B_0^{3/2}$, we can estimate the minimum and the maximum values from the difference between our measured and computed signals in the sum-of squared residuals statistic.

To carry out this estimate, we use Matlab to find the minimum difference between our theoretical model and our experimental data as the fitting parameter is varied, and we plot the sum of squared residuals, S , as a function of the fitting parameter as we have earlier in this section. We quantify the noise, and add $\pm 1\sigma$ confidence intervals for S , using the $\pm 1\sigma$ width of the sum of squared error (SSE) curve to define the error in the fitting parameter.

As an example, we apply this procedure to find the error estimate for the rotational constant $B_0^{1/2}$ at a pressure of 100 mmHg. This will serve as describing a representative calculation, and can be applied directly to find the error in the estimates of $B_0^{1/2}$ at different pressures, as well as the errors associated with extracting the other fitting parameters. The mathematical details of the calculation are presented in Appendix A.

In Figure 15, the SSE is plotted as in previous sections as the red curve. Introducing the quantified statistical error, the $\pm 1\sigma$ confidence intervals are plotted in blue (above) and green (below), respectively.

The range of possible values that we take as the error in the fitting parameter is obtained by the intersection of a horizontal line through the minimum of the $+1\sigma$ SSE curve with the -1σ SSE curve. The error in best-fit values for all fitting parameters is reported in an identical manner in this thesis.

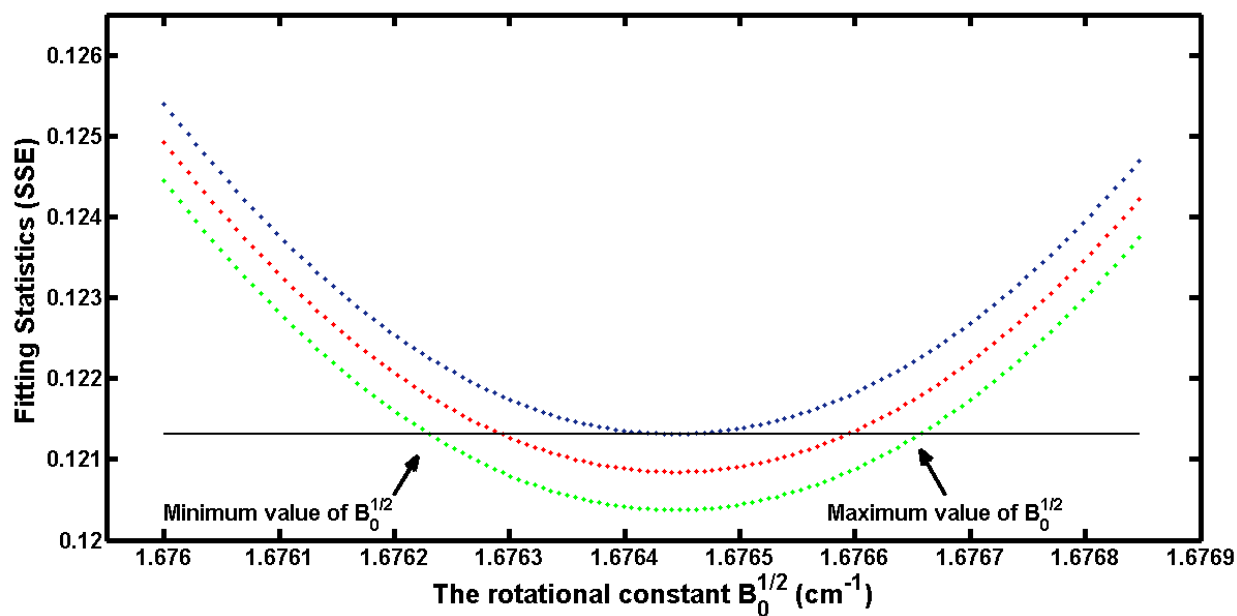


Figure 15. Fitting of $B_0^{1/2}$ at pressure $p = 750$ mmHg. With best fitting for $B_0^{1/2}$ (red), best fitting for $B_0^{1/2} + 1\sigma$ (blue), and best fitting for $B_0^{1/2} - 1\sigma$ (green).

4.2.5 Comparison of model and experimental data

Once all of the fitting parameters are obtained by iterating the fitting procedure to convergence as outlined in the previous sections, the goodness-of-fit can be looked at to see how well the model actually describes the experimental data. As an example, both the model and the experimental data for THz-TDS of NO at $p = 525 \pm 5\%$ mmHg are illustrated in figure 16:

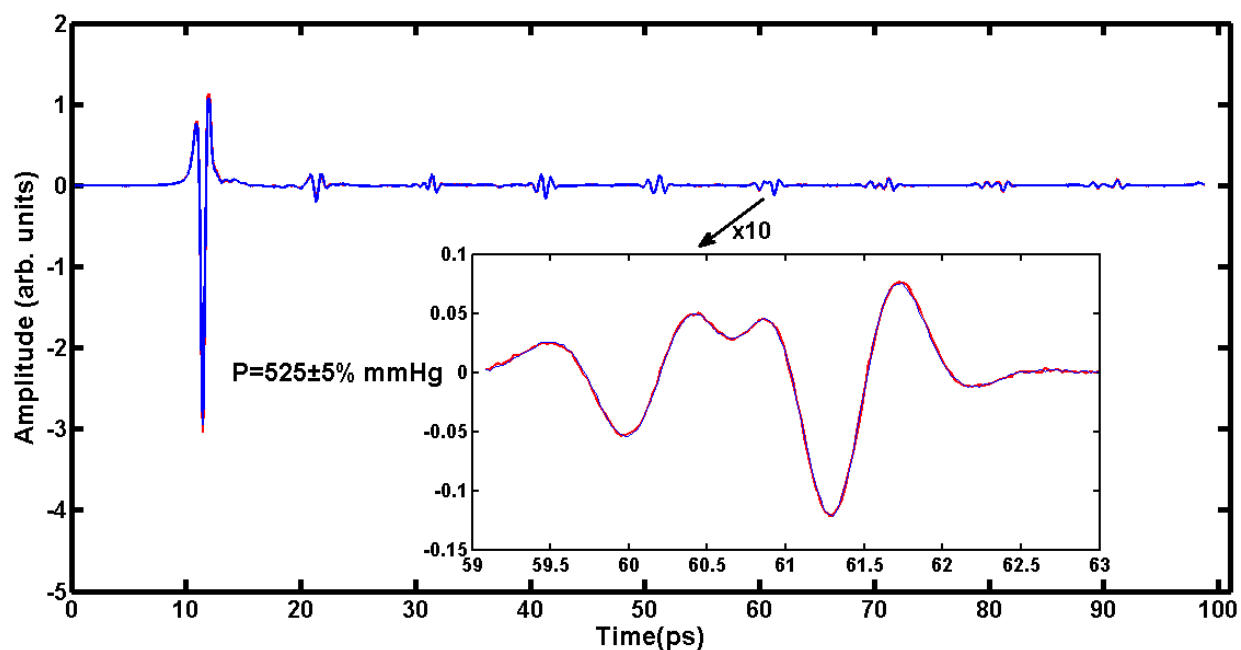


Figure 16. THz scan of NO at partial pressure of $p = 525 \pm 5\%$ mmHg (with total pressure of 1 atm). Model waveform is shown in red, data waveform in blue, with an inset of an echo located around 61ps.

By plotting the residuals (the difference between our theoretical model and our experimental data as it is shown in figure 16), we can check to see if there are any systematic errors in the fitting procedure. One would expect simple noise in the residuals if the fitting procedure was working as expected, whereas a systematic difference would indicate a problem with the fitting procedure.

The residuals from the best fit for all four free parameters are shown in figure 17 below (for NO at $p = 760$ mmHg). As can be seen from the residual (shown in purple), the differences are mostly small with no systematic error compared to the electrical background noise (shown in black in the inset). However, there is a notably larger residual during subsequent echoes which possibly results from an imperfect alignment of the signals in time because of the finite grid spacing in time. Note that the signal level is three orders of magnitude larger than the residual (comparing the y-axis of Figures 16 and 17), noting that while the y-axis scale is arbitrary, the units are relative between Figures 16 and 17.

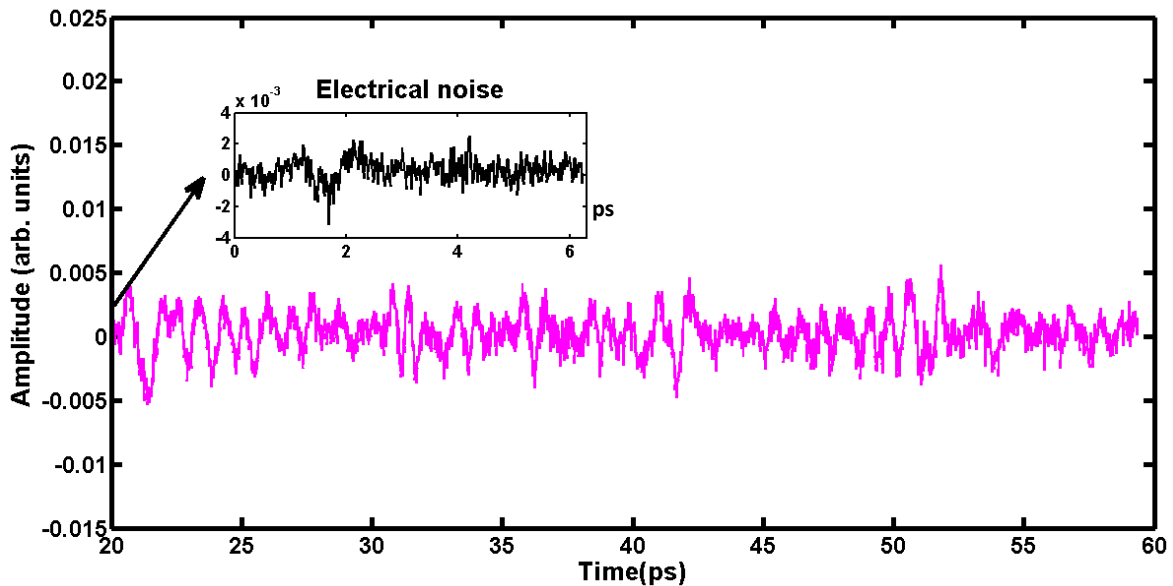


Figure 17. Residual between model and data for NO at $p = 760$ mmHg. The inset shows the electrical noise in the measured signal before the main THz pulse.

The residual amplitude (purple) is close to the electrical noise amplitude (black), therefore, we conclude the fitting procedure is valid and working well. With confidence in the model, we can now turn our attention to looking at how the THz response of NO scales with pressure in order to be able to project limits of detection.

4.3 Pressure scaling

In this part of my thesis, we will apply the theoretical model of the interaction between THz radiation and NO at different partial pressures up to approximately 1 atmosphere of NO in increments 50 mmHg. Reference measurements and sample measurements are made at each pressure, and the model is applied to extract best-fit parameters as described in the previous sections.

The pressure of NO is varied experimentally as follows. A specific amount (e.g. 100 mmHg) of NO gas is introduced into the gas-cell, then nitrogen gas (N₂) is added to the gas cell until a total pressure of 760 mmHg is achieved. Bringing the total system pressure to be around 1 atm serves two purposes. First, it simulates measurements of NO in ambient conditions, allowing a valid extrapolation to detection limits. Second, it is expected that the collisional time (impacting the collisional rephasing of the system) depends on total pressure of the system (i.e. fitting parameter τ_c).

By keeping the total pressure constant, it was expected that this fitting parameter τ_c would also remain constant during the various experiments. The latter point will be revisited, as it will be shown not to be the case. A schematic diagram of the gas filling system is shown in figure 18. A vacuum system is attached to the gas cell, allowing the cell to work under vacuum.

A fixed partial pressure of NO can be introduced to the gas cell by simply opening the NO valve and monitoring the pressure measured by the attached pressure gauge. Subsequently, N₂ can be added to bring the total system to 1 atm of pressure by opening the valves on the N₂ side of the system.

In other words, our target is to keep NO at a specific pressure (e.g. take $p = 100$ mmHg) during the acquisition of a set of experimental data, but the challenge is how to open the gas-cell valve again (to add the N₂, so we can reach a total system pressure of 1 atm) while preventing the NO from escaping outside of our gas-cell (which will cause an error in our pressure measurements). So, to overcome this issue, we used a high pressure N₂-gas cylinder (of a few thousand mmHg). This high pressure of N₂ will force NO to stay inside the gas-cell, and by controlling the N₂ valve, we can allow a specific amount of N₂ (e.g. take $p = 660$ mmHg of N₂) until we reach a total pressure (of the mix between NO and N₂) of 1 atm inside the gas-cell.

Because of the procedure used for gas filling where two valves were opened simultaneously to allow N₂ into the system, the uncertainty in pressure introduced a $\pm 5\%$ error in our pressure measurements. This 5% value comes from the fact that the volume of the connecting tubes is around 10.2% of the volume of the gas-cell, and depending on how the valves were opened, could introduce between 0 and 10.2% error. We therefore take $\pm 5\%$ error as a reasonable estimate of the introduced error. For example, if the reading of the NO inside the gas cell is equal to 100 mmHg, we take a pressure of $96 \pm 5\%$ mmHg for the model, which covers all of our 10.2% error range. For this reason, we have horizontal error-bars for our pressure measurements in the forthcoming graphs.

Experimental procedure summary for gas-mixing

- 1- Open the valve-1 and valve-4, and make sure it is connected to vacuum system as shown.
- 2- Open valve-4 of vacuum pump to keep the gas-cell under vacuum. Then close it.
- 3- Open valve-2 of NO until we reach the required pressure inside the gas-cell, then close it.
- 4- Close the valve-1 of the gas-cell.
- 5- Turn on the vacuum pump, to make sure there is no more NO inside the connector tubes.
- 6- Open “valve-3 of N₂“ and “valve-1 of the gas-cell” simultaneously, letting N₂ into the cell until we reach 1 atm total pressure. Finally, close valve-1 and start our THz scanning.

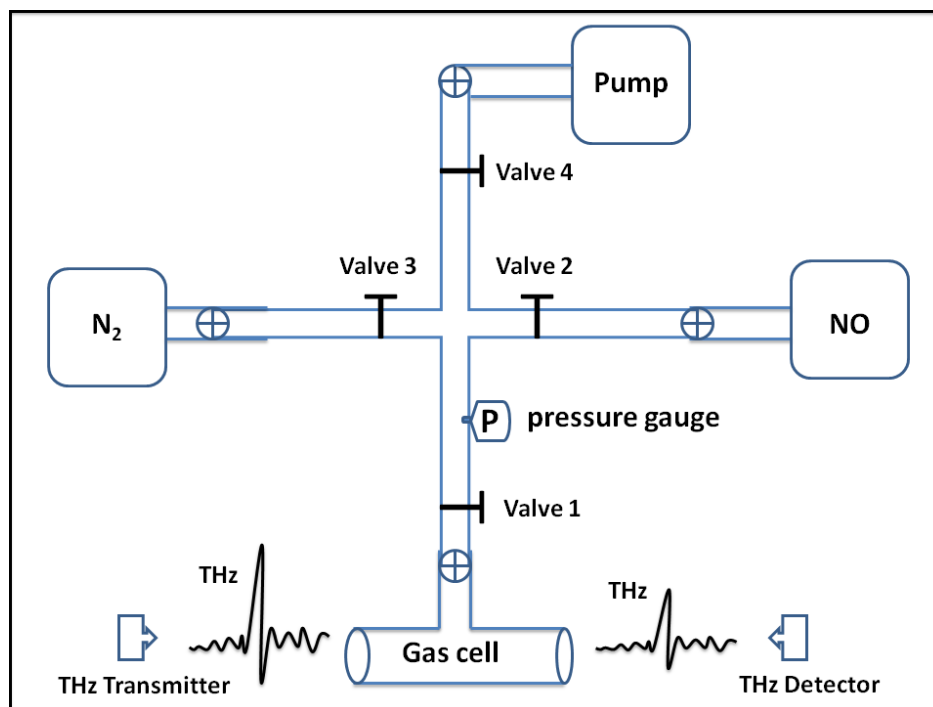


Figure 18. Schematic diagram for NO and N₂ gas mixing.

Using this procedure, other partial pressures of NO (between 50 mmHg and 750 mmHg in 50 mmHg increments) were studied, the fitting process applied, and the physical parameters extracted for each pressure. The results are presented in the next section.

4.4 Experimental results and analysis

We have already developed a theoretical model (in chapter 3), which we can use to extract the physical parameters of NO. The next part of my thesis will show the experimental results, and compare to our theoretical model.

A long scan (~200 ps) of NO at a pressure of 760 mmHg (1 atm) is shown in figure 19, where we have our model waveform in red and our collected data is in shown in blue. This scan is important because it is for pure NO-gas so we have a certainty about the pressure (we take it as 760 mmHg). This allows us to extract the physical parameters (e.g. the centrifugal stretching constant of the ground vibrational states (${}^2\Pi_{1/2}$ and ${}^2\Pi_{3/2}$), $D_0^{1/2}$ and $D_0^{3/2}$ in Equation 15), which we will fix to be constant during the fitting procedure of the other parameters at different pressure scales. That is, the centrifugal stretching constant is assumed to be independent of pressure. We find the best fit values of the centrifugal stretching constant for the two NO states ${}^2\Pi_{1/2}$ and ${}^2\Pi_{3/2}$ to be:

$$D_0^{1/2} = (2.0326 \pm 2.77) \times 10^{-7} \text{ cm}^{-1}, \text{ and } D_0^{3/2} = (10.405 \pm 1.26) \times 10^{-6} \text{ cm}^{-1}$$

Which compare well to published literature values for the centrifugal stretching constant [45]:

$$D_0^{1/2} = (3.40 \pm 3.0) \times 10^{-7} \text{ cm}^{-1}, \text{ and } D_0^{3/2} = (10.240 \pm 0.23) \times 10^{-6} \text{ cm}^{-1}$$

Our values therefore are consistent with the literature values within error margin. The calculations of the error in $D_0^{1/2}$ and $D_0^{3/2}$ is carried out the same way as shown before in section 4.2.4 (statistical error analysis). As the value of $D_0^{1/2}$ and $D_0^{3/2}$ is small compared to our statistical error (which is calculated in terms of the electric noise floor), we have a large uncertainty of the

exact values of $D_0^{1/2}$ and $D_0^{3/2}$. That is, the SSE curve is very broad rather than sharp as was the case for the rotational constant shown in the statistical error analysis section.

Therefore, by using these to values of the centrifugal stretching constant in our theoretical model, we can plot the two waveforms together as presented in figure 19 below:

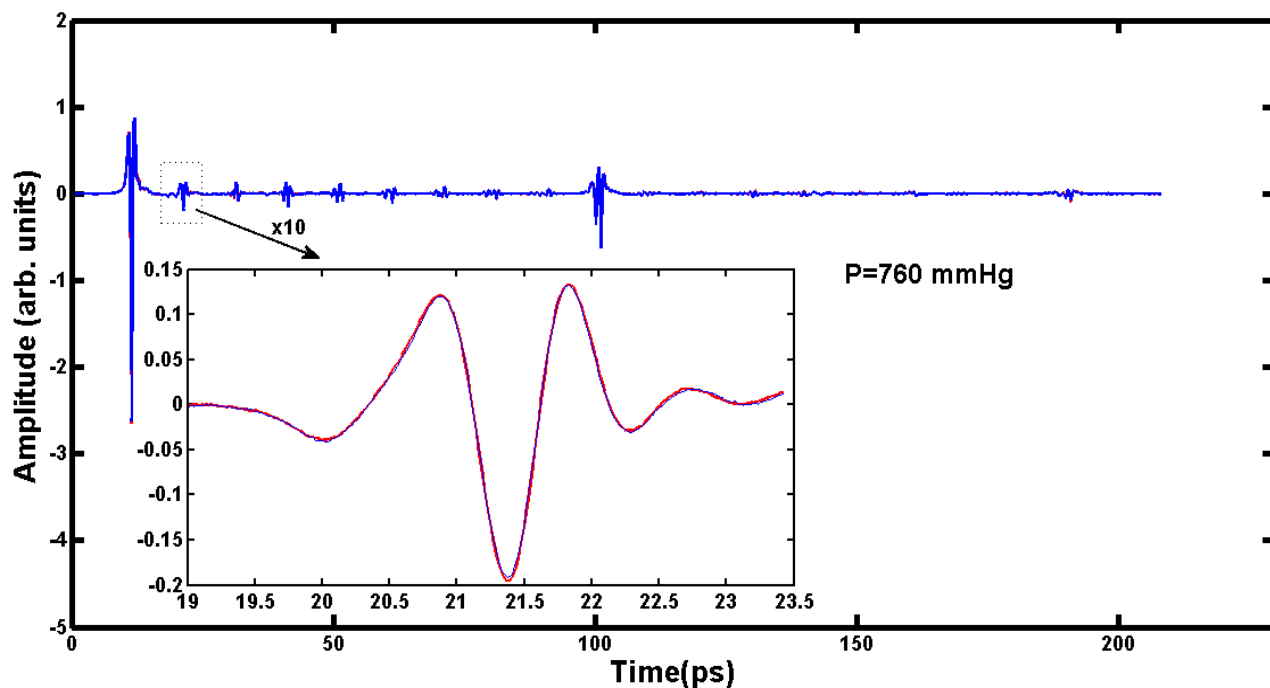


Figure 19. A long 200 ps scan for NO at atmospheric pressure of 760 mmHg. The model waveform is shown in red, and the measured data is shown in blue.

It is interesting to look at the echoes and relate their structure to the physical behavior of NO. At earlier times (closer to the main THz peak), the echoes appear as one pulse with a complicated pattern, which results from the complex beating of the individual echoes from the manifold of transitions of each of the two electronic states of NO (${}^2\Pi_{1/2}$ and ${}^2\Pi_{3/2}$).

Interestingly, at later times, because the rotational constant for the two electronic states is different, the individual echoes become separated in time, and the echoes of the individual electronic states become identifiable.

As an example, we plot both the model and the NO-scan for three different pressures (96, 430 and 717±5% mmHg) on the same graph with a vertical offset for the 430 mmHg and 717 mmHg scans as shown in figure 20 below.

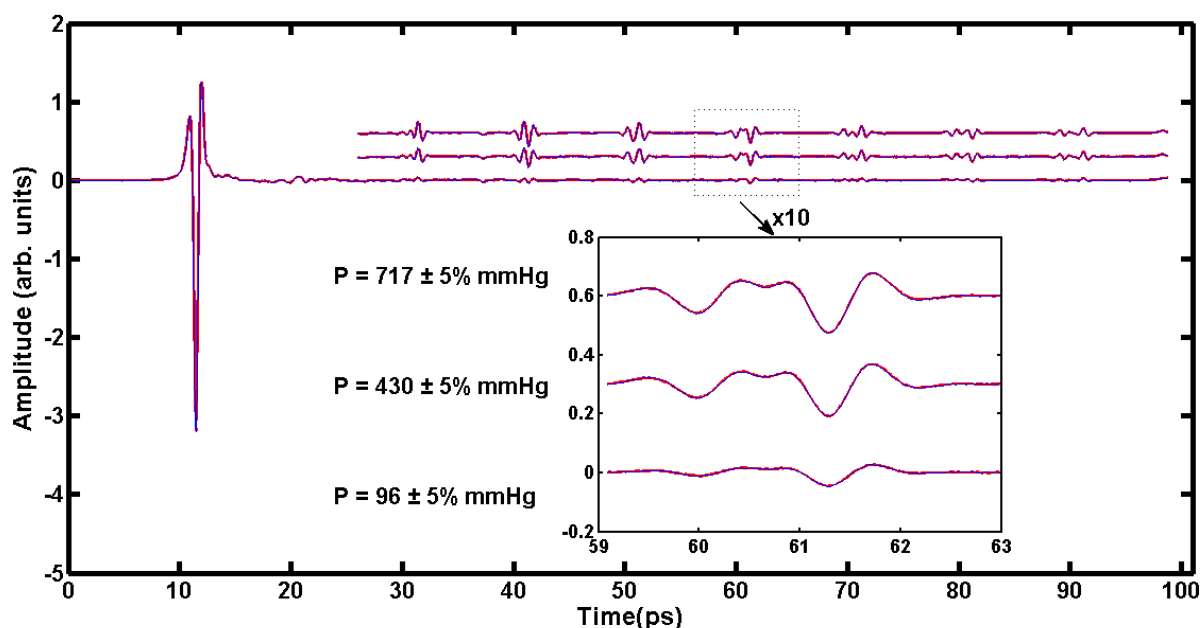


Figure 20. NO model (red) and data (blue) waveforms at a pressure of 100 mmHg, showing echoes for pressures around 100, 450 and 750 mmHg. The larger pressure curves in the vicinity of the echoes are offset for clarity, and placed on an expanded scale in the inset so that the excellent fit is visible. As expected, the peak height of the echoes increases with increasing pressure. This trend is observable for the all measured NO pressures (100 – 750 mmHg).

4.4.1 The results of the rotational constant $B_0^{1/2}$ and $B_0^{3/2}$

In Table 4, the results for the rotational constant at different partial pressures of NO is presented. The estimated error is also given, which is calculated as described previously in section 4.3. The error in all pressure measurements is $\pm 5\%$ mmHg, and results from the procedure used for introducing partial pressures of NO into the gas cell with the valving system described previously. As can be seen in table 4, the rotational constants for the two electronic states do not vary significantly over the tested pressure range, and are consistent with published values (as shown before in table 3).

Table 4. The rotational constant for the two electronic states (${}^2\Pi_{1/2}$ and ${}^2\Pi_{3/2}$) with respect to change of the NO partial pressure.

The Pressure $P \pm 5\%$ (mmHg)	The Rotational constant $B_0^{1/2} (\times 10^{10}) \text{ cm}^{-1}$	The Rotational constant $B_0^{3/2} (\times 10^{10}) \text{ cm}^{-1}$
96	1.6762 ± 0.00058	1.7247 ± 0.00120
143	1.6763 ± 0.00046	1.7248 ± 0.00093
191	1.6762 ± 0.00036	1.7246 ± 0.00070
238	1.6763 ± 0.00031	1.7248 ± 0.00060
287	1.6763 ± 0.00028	1.7248 ± 0.00053
334	1.6762 ± 0.00001	1.7248 ± 0.00056
382	1.6763 ± 0.00028	1.7248 ± 0.00051
430	1.6763 ± 0.00026	1.7249 ± 0.00050
478	1.6763 ± 0.00046	1.7248 ± 0.00045
525	1.6763 ± 0.00025	1.7248 ± 0.00043
573	1.6763 ± 0.00023	1.7248 ± 0.00041
621	1.6763 ± 0.00021	1.7249 ± 0.00035
669	1.6764 ± 0.00018	1.7249 ± 0.00031
717	1.6763 ± 0.00016	1.7248 ± 0.00028

It is useful to plot the effect of changing the pressure on the rotational constants of the ground vibrational state (${}^2\Pi_{1/2}$ and ${}^2\Pi_{3/2}$), $B_0^{1/2}$ and $B_0^{3/2}$ with respect to changing the pressure from 100 mmHg to 750 mmHg, as shown below in figures 21 and 22, and also comparing to some of the published literature values.

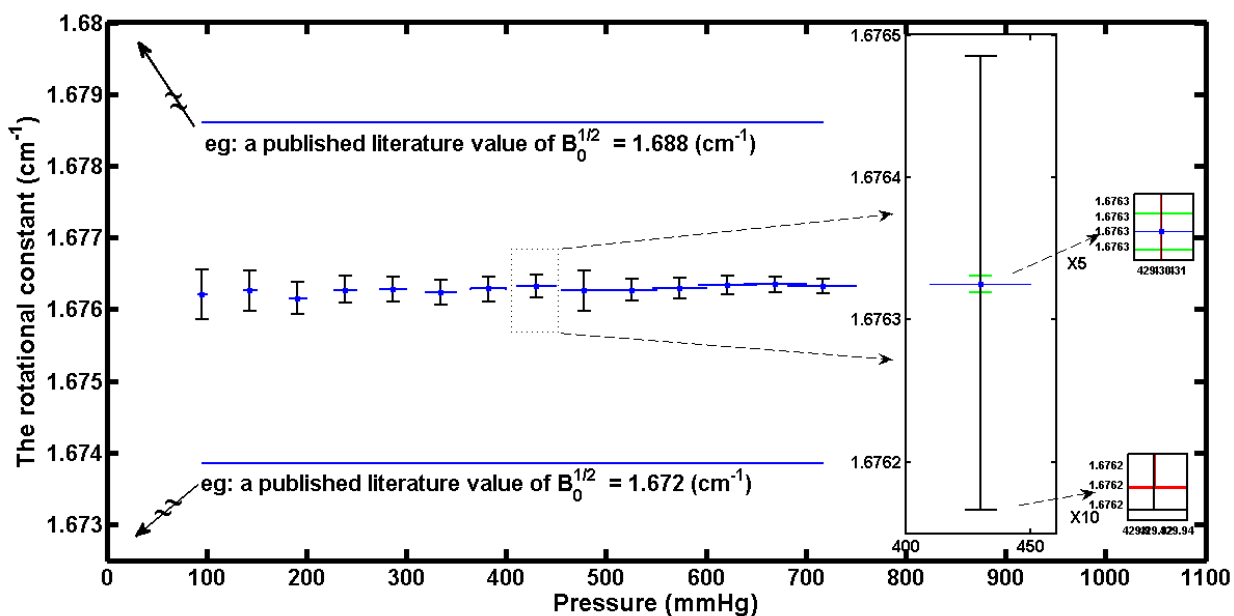


Figure 21. The change of $B_0^{1/2}$ with pressure and compared to literature values. The associated error is shown on the expanded scales on the right. The horizontal (blue) error bars cover the uncertainty in measuring the pressure, the vertical (green) error bars cover the uncertainty in measuring $B_0^{1/2}$ due to the pressure error, and the vertical (red) error bars cover the uncertainty in measuring $B_0^{1/2}$ due to the statistical error (system electrical noise floor). The black error bar represents the sum of statistical and pressure error added in quadrature as described in the text.

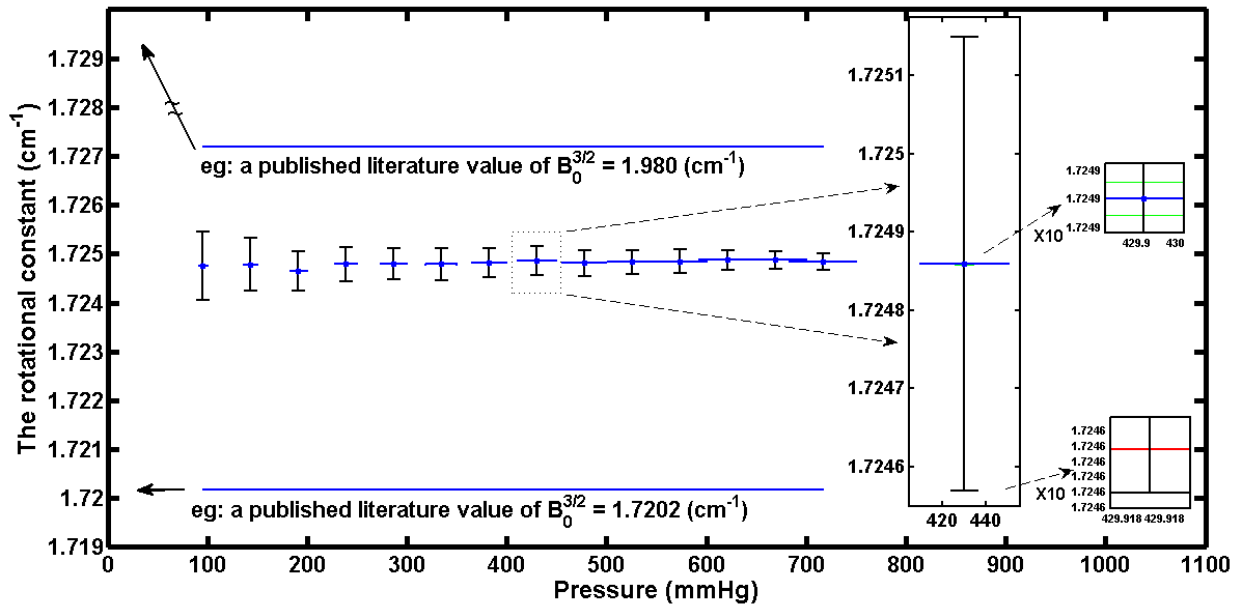


Figure 22. The change in $B_0^{3/2}$ with pressure and compared to literature values. The associated error is shown on the expanded scales on the right. The horizontal (blue) error bars is to cover the uncertainty in measuring the pressure. The vertical (green) error bars is to cover the uncertainty in measuring $B_0^{3/2}$ due to the pressure error. The vertical (red) error bars is to cover the uncertainty in measuring $B_0^{3/2}$ due to the statistical error (system electric noise floor). The vertical (black) error bars are calculated by adding both the green error-bar and the red error-bar in quadrature.

In figure 21 and figure 22, it is clear that the rotational constant is approximately constant over the pressure range considered (within error). The values for the rotational constant are well within the range of published values. The error bars on our values are obtained as follows. The horizontal error bars (shown in blue) are $\pm 5\%$ of the measured pressure, which is the uncertainty in our pressure measurements as a result of the gas filling procedure described previously.

Also we have two different vertical error bars which are included to show the relative contributions. The first error-bar (green), which covers all of the possible values of $B_0^{1/2}$ and $B_0^{3/2}$ under the effect of considering the maximum pressure or the minimum pressure with respect to the middle pressure (which is our middle data points), and the second error-bar (red) which covers all of the possible values of $B_0^{1/2}$ and $B_0^{3/2}$ considering the effect of the electrical noise of our system as described in section 4.2.4.

For example, for $p = 96 \pm 5\%$ mmHg, we use three different possible values for the pressure (i.e. the maximum pressure $p_{max} \cong 100$ mmHg, the middle pressure $p_{mid} \cong 96$ mmHg, and the minimum pressure $p_{min} \cong 91$ mmHg). For each one of these three pressures, the fitting procedure is used to find the best fit value of $B_0^{1/2}$ and $B_0^{3/2}$ (i.e. we will get the values of $B_{0_{max}}$, $B_{0_{mid}}$, and $B_{0_{min}}$), where these three values of $B_0^{1/2}$ and $B_0^{3/2}$ are covered by the green error-bars in Figures 21 and 22.

The red error bars are calculated as described in *section 4.2.4*, so we can cover all of the possible values of $B_0^{1/2}$ and $B_0^{3/2}$ by accounting for the background electrical noise in our calculations. Both of these two errors affect the measurements of $B_0^{1/2}$ and $B_0^{3/2}$ (i.e. pressure error, σ_P , and statistical error, σ_{St}). Then, these two errors are added together in quadrature to give the total error, σ_{Total} , shown as the black vertical error bar in Figures 21 and 22:

$$\sigma_{Total} = \sqrt{\sigma_P^2 + \sigma_{St}^2} \quad (23)$$

Also, as we can see in figure 21 and in figure 22, the error-bars decrease with increasing pressure, which is because at the higher partial pressures of NO, the echo height is large relative to the electrical ground noise, so we have high certainty in our results. But at the lower pressure, the echo height is close to the electrical noise floor, which leads to a larger error.

As a comparison, if we plot figure 21 and 22 of $B_0^{1/2}$ and $B_0^{3/2}$ together in one graph, as shown in figure 23, we can see the change in $B_0^{1/2}$ and $B_0^{3/2}$ with respect to pressure change, and compare it to some of the published literature values (*we can see that our measurements are located among the published values*), with error bars as described before and shown in figures 21 and 22.

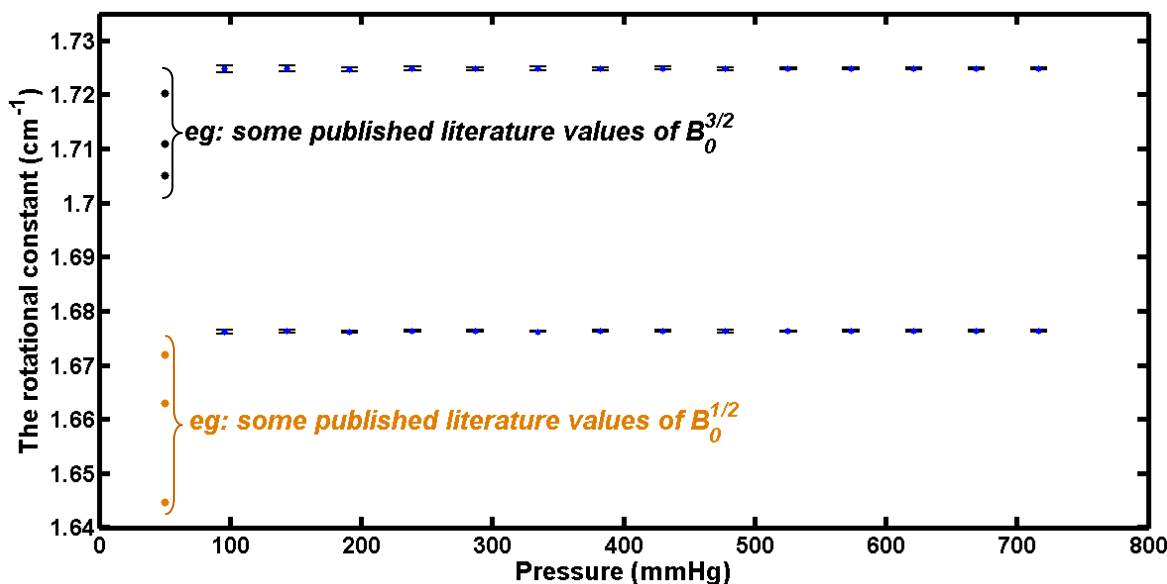


Figure 23. The change in $B_0^{1/2}$ and $B_0^{3/2}$ with pressure and compared to literature values. The error bars on the data points are as calculated in figures 21 and 22. A selection of published literature values of $B_0^{1/2}$ and $B_0^{3/2}$ are shown in brown and black dots respectively.

4.4.2 The results of the angular frequency linewidth

In Table 5, we present the experimental results of the angular frequency linewidth, $\Delta\omega$. As we described before in Equation 14, the FWHM is directly related to the collisional time $\tau_c = \frac{1}{\Delta\omega_j}$. Since there are two different states for NO (${}^2\Pi_{1/2}$ and ${}^2\Pi_{3/2}$), we modified our Matlab fitting model to check if it is possible to find a distinguishable difference between the collisional time of these two different NO states, which would then have FWHMs of $\Delta\omega_{1/2}$ and $\Delta\omega_{3/2}$,

Table 5. The change in the angular frequency linewidth $\Delta\omega$, $\Delta\omega_{1/2}$, and $\Delta\omega_{3/2}$ with respect to the change in NO partial pressure.

Pressure P \pm 5% (mmHg)	$\Delta\omega$ ($\times 10^{10}$) (rad./s)	$\Delta\omega_{1/2}$ ($\times 10^{10}$) (rad./s)	$\Delta\omega_{3/2}$ ($\times 10^{10}$) (rad./s)
96	1.417 \pm 0.42	1.338 \pm 0.46	1.688 \pm 0.93
143	1.493 \pm 0.33	1.412 \pm 0.36	1.769 \pm 0.73
191	1.523 \pm 0.25	1.457 \pm 0.27	1.740 \pm 0.53
238	1.582 \pm 0.22	1.521 \pm 0.25	1.777 \pm 0.46
287	1.583 \pm 0.19	1.516 \pm 0.22	1.794 \pm 0.41
334	1.547 \pm 0.21	1.478 \pm 0.23	1.760 \pm 0.42
382	1.617 \pm 0.19	1.546 \pm 0.22	1.830 \pm 0.40
430	1.656 \pm 0.18	1.589 \pm 0.21	1.853 \pm 0.37
478	1.676 \pm 0.17	1.611 \pm 0.19	1.865 \pm 0.35
525	1.699 \pm 0.16	1.635 \pm 0.19	1.878 \pm 0.33
573	1.783 \pm 0.15	1.715 \pm 0.18	1.969 \pm 0.31
621	1.972 \pm 0.14	1.899 \pm 0.15	2.166 \pm 0.27
669	2.224 \pm 0.12	2.146 \pm 0.13	2.428 \pm 0.23
717	2.489 \pm 0.11	2.406 \pm 0.12	2.704 \pm 0.21

The values presented in Table 5 show that we can find a slightly different value for the collisional time between the two different states for NO (${}^2\Pi_{1/2}$ and ${}^2\Pi_{3/2}$). These results can be visualized more effectively by plotting the effect of changing the pressure on $\Delta\omega$, as shown below in figure 24 and also by plotting the effect of changing the pressure on $\Delta\omega_{1/2}$, and $\Delta\omega_{3/2}$ as shown in figure 25.

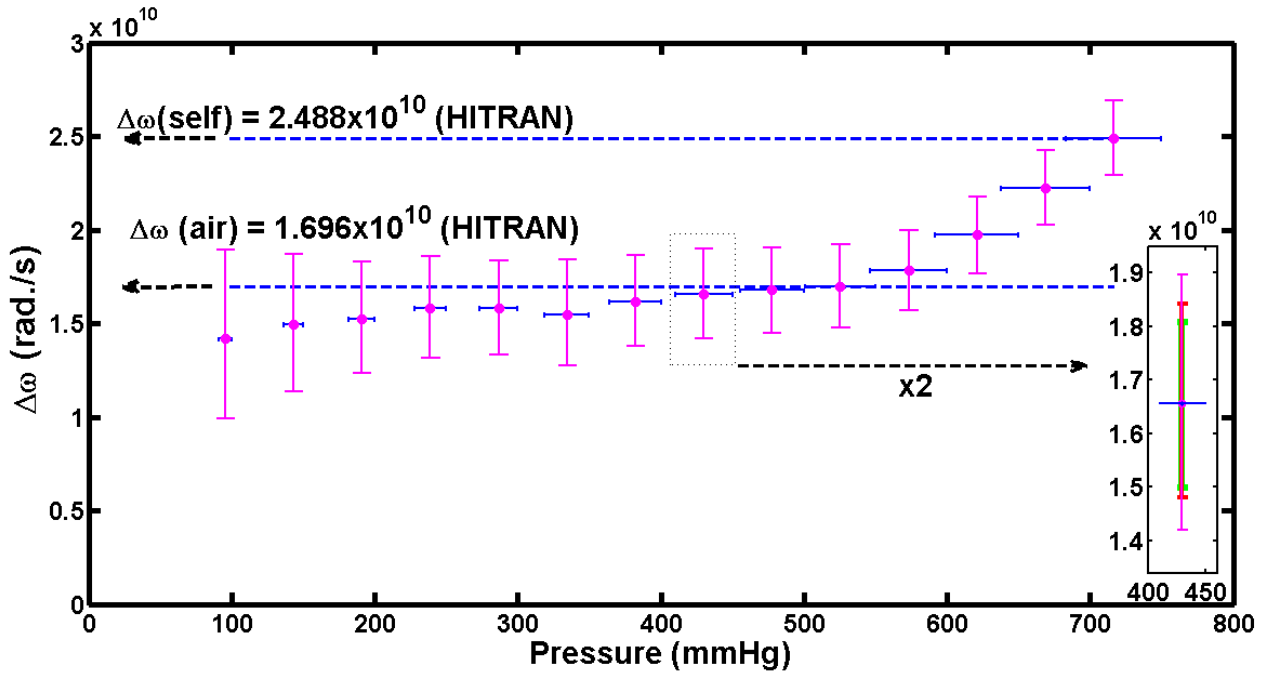


Figure 24. The change in the angular frequency line width $\Delta\omega$ with respect to the pressure change compared to literature values (HITRAN Database shown in dashed blue lines), with vertical error-bars for $\Delta\omega$ (purple) and horizontal error-bars of the pressure (blue). The inset shows the error bars at a pressure of $p = 430$ mmHg, where the vertical (green) error bars cover the uncertainty in measuring $\Delta\omega$ due to the pressure error, and the vertical (red) error bars cover the uncertainty in measuring $\Delta\omega$ due to the statistical error (system electrical noise floor).

The error bars in figure 24 are obtained in the same way as described in the last section. The horizontal error bars reflect the error in pressure of $\pm 5\%$ from the method used to introduce NO partial pressures. Vertical error bars combine the statistical error from noise in the system (green) and the uncertainty introduced into the best-fit values from the uncertainty in pressure (pink). Also, from Table 5, and by accounting for the two different states of NO ($^2\Pi_{1/2}$ and $^2\Pi_{3/2}$), we can plot a graph which shows the effect of changing the pressure on $\Delta\omega_{1/2}$ and $\Delta\omega_{3/2}$ (which reflect the values of the collisional time τ_c for the two different states of NO: $^2\Pi_{1/2}$ and $^2\Pi_{3/2}$). The results can again be compared to published literature values provided in the HITRAN Database [48] and are shown below in figure 25.

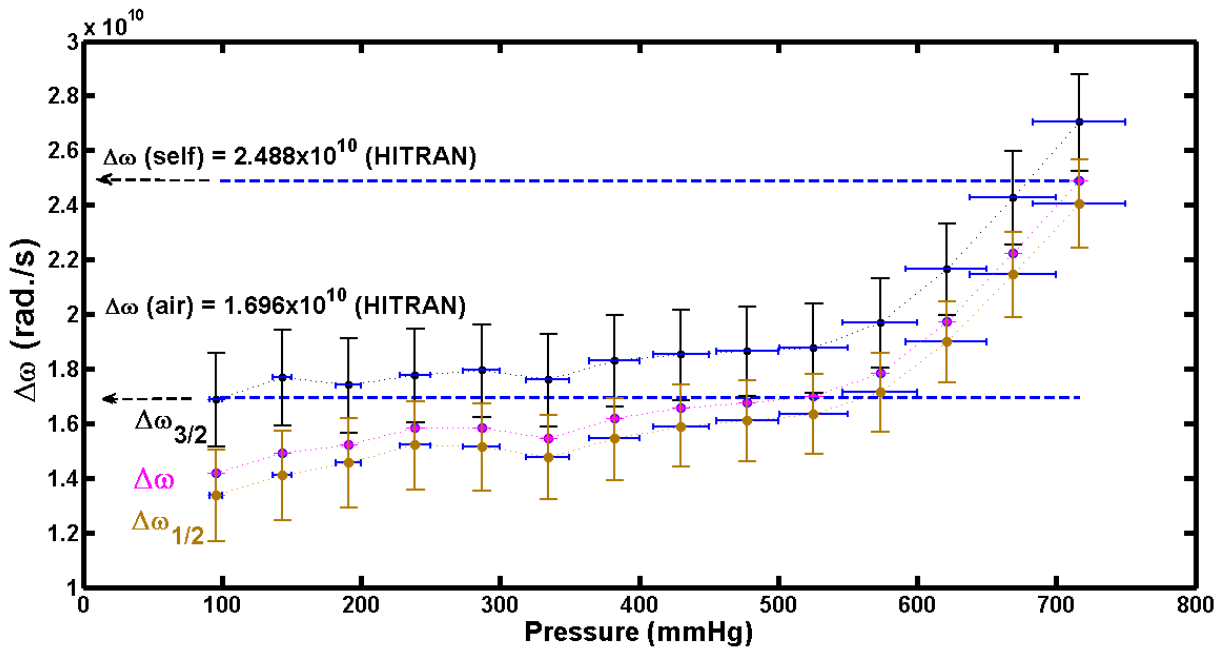


Figure 25. The change in $\Delta\omega$, $\Delta\omega_{1/2}$ and $\Delta\omega_{3/2}$ with respect to the pressure change compared to literature values (HITRAN Database shown in dashed blue lines). with horizontal error-bar of the pressure (blue). $\Delta\omega$ (purple), $\Delta\omega_{1/2}$ with vertical error-bars (brown) and $\Delta\omega_{3/2}$ with vertical error-bars (black). The error-bars represent the sum of statistical and pressure error added in quadrature.

In figure 25 the larger error at lower pressures results from the reduced signal to noise ratio of the echo measurements at low pressure. At higher pressures, the background electrical noise is very small compared to the echo amplitude, so the fitting is more accurate at the higher pressures.

Furthermore, in figure 25 we found a good correlation between our results and those reported in the HITRAN database. Specifically for the cases of air- and self-broadening values of the angular frequency linewidth. The air-broadening value represents our NO measurements at low-pressure (around 100 mmHg), where the gas-cell is filled with N₂ (more than 650 mmHg), so we consider that our gas-cell is almost filled with air, and for this to be reflected in the angular frequency linewidth as the air-broadened value, consistent with what we find.

In the same way, the self-broadened value is represented in our NO measurements at high pressure (around 750 mmHg), where the gas-cell is almost completely filled with NO (with less than 10 mmHg of N₂), and we therefore expect to observe the self-broadened linewidth consistent with what we observe.

In figure 25, we are also able to distinguish between the two different collisional times for $NO_{(2\Pi_{1/2})}$ and $NO_{(2\Pi_{3/2})}$ in terms of the two different angular frequency linewidths, $\Delta\omega_{1/2}$ and $\Delta\omega_{3/2}$, where the value obtained by using only one angular frequency $\Delta\omega$ in the model is located within the error-bars of these two collisional times.

This makes sense physically, because NO has two different states ${}^2\Pi_{1/2}$ and ${}^2\Pi_{3/2}$, and each state will have a different collisional time due to having different energy, and therefore a different valence electron structure, and subsequently a different collisional cross-section. In this case, we would expect the higher energy state to exhibit a larger cross section overall. As such, the higher energy state would exhibit a smaller collisional time, and therefore a larger angular frequency linewidth (because the linewidth is inversely proportional to the collisional time).

These observations are consistent with the observed larger linewidth for $\Delta\omega_{3/2}$. But as we can see from figure 25, our error-bars are quite large (where the $\Delta\omega_{1/2}$ error-bars almost intersect the $\Delta\omega_{3/2}$ error-bars), so we cannot draw this conclusion with high confidence, but simply note that it is consistent with what is expected. That our THz-TDS appears to be able to find a difference between the collisional time of the two different Π -states of NO is something that has not previously been reported in the literature and is interesting.

Another interesting point is that, while working at different partial pressures of NO, we expected the collisional time be constant when maintaining a fixed total system pressure. That is, the time constant should be independent of the NO pressure so long as the total pressure inside the gas-cell is kept constant (around 1 atm). Experimentally, we realized that the collisional time constant (equivalent to the angular frequency linewidth as they are inversely proportional) decreases with increasing partial pressure of NO.

After comparing to the HITRAN database values, it is clear that the experimentally observed change with NO partial pressure should occur because the cross-section of NO with itself (self-broadened value) is larger than the cross-section of NO with N₂ collisions (air-broadened value).

The expected air- and self-broadening values are also expected based on the total collision cross-sections for NO and N₂ which have been measured by the scattering of beams of K and Cs by a variety of scattering molecules as summarized in Table 6 from [49] and [50].

Table 6. Total collision cross sections for NO and N₂ with atomic beams of K.

Molecule	μ (D)	Q-Calculated (cm²)	Q-Observed (cm²)
N ₂	0	1	0.97
NO	0.15872	1	1.06

Here, μ is the dipole moment and Q is the total collision cross section (calculated and measured). As shown in Table 6, the collisional cross section for K with NO is slightly larger than with N₂, again consistent with what we observe and what is reported in the HITRAN database for the air- and self-broadened linewidths from NO spectroscopy.

In figure 26, an exaggerated diagram of the NO-N₂ gas mixing, with the imaginary physical size of the molecules representing the collisional cross sections is presented.

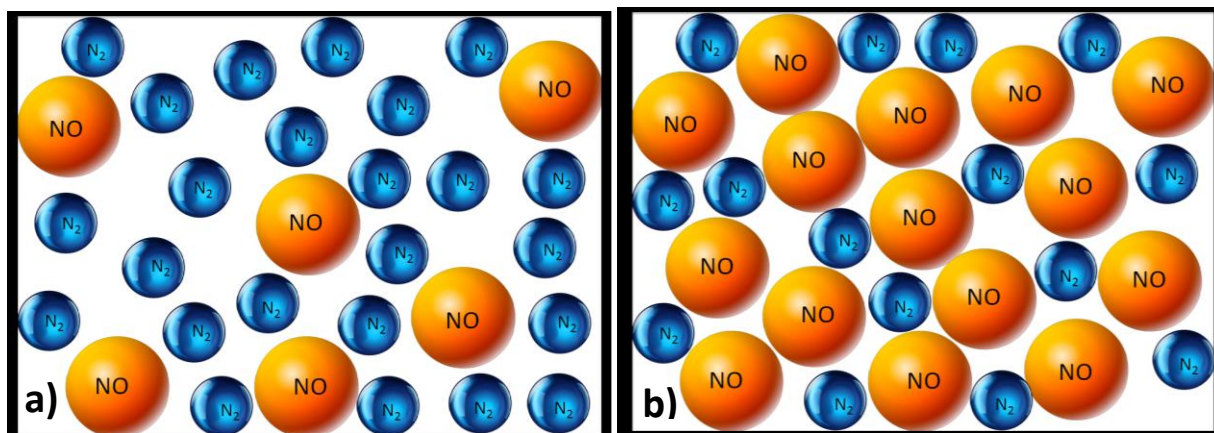


Figure 26 (a). Example of low partial pressure of NO, and figure 26 (b). Example of large partial pressure of NO. where the total pressure of NO in figure (a) and (b) is kept constant (at 1 atm). The size of the molecules is meant to represent the collisional cross section (exaggerated).

At the same total pressure (for example 1 atm), we have different inter-particle spacing between NO and N₂ due to having different cross-sections and this affects the time between collisions, which is inversely proportional to the angular frequency linewidth.

In other words, if we have a fixed number of particles enclosed in a gas-cell, as we replace the smaller cross-section N₂ molecules by the larger cross-section NO molecules, and under the condition that the number of particles kept constant (as the pressure is kept constant at 1 atm), the inter-particle spacing will decrease and the collisional time subsequently decreases.

Ultimately, we are interested in determining the limit of detection for this new type of measurement. In order to determine the limit of detection in partial pressure for NO using THz-TDS, it is necessary to understand how the echo heights scale with pressure. In order to do this, we measured the heights of the echoes in terms of their peak-to-peak height, and compare how

these values scale with pressure in the theoretical model and the experimental data. The scaling will then be used to project the ultimate limits of detection.

The peak-to-peak echo-height is shown in figure 27 below as a function of the NO partial pressure. In this case, we are studying the third echo (also, we can apply the same rules for the other echoes we have). It should be noted that the scaling for all echoes at low pressure is approximately linear, however, the scaling deviates from linear at larger pressures.

The peak-to-peak echo height is scaled to the Root Mean Square (RMS) reference electric field of the sample waveform before the main pulse (i.e. to plot the signal to noise ratio). This RMS was computed using the 250 available reference data points collected before the initial pulse of the sample signal which is found to be 0.0016 (in arbitrary units). The ratio between the echo height and the RMS is then given by:

$$E_{pk-pk} = \frac{E_{echo}}{E_{rms}} \quad (24)$$

Where we measured the echo height (E_{echo}) manually by finding the difference between the higher and the lower value of the echoes (from our experimental data points) and also we can measure the echo height manually from the model waveform obtained. The manual calculation is carried out by using Matlab, plotting the echoes, and extracting the echoes height values from the plot by hand. But due to our uncertainty in measuring the echo heights manually, we estimate the error associated with the extraction (assumed to be 0.2% of the echo height), which is obtained by making multiple measurements by hand and taking the standard deviation of the measurements. The results are reported with error bars in figure 27 and 28.

By using Matlab, we can measure these heights in terms of relative ratio to the reference value. The peak-to-peak values for the third echoes are presented in Table 7.

Table 7. The peak-to-peak ratio of the 3rd echo with respect to the change in pressure.

Pressure P ± 5% (mmHg)	Peak to Peak (E_pk-pk 3rd echo)/E_rms (arb. units)
96	34.60
143	51.90
191	71.87
238	88.55
287	105.44
334	111.57
382	125.26
430	139.05
478	160.18
525	174.19
573	186.09
621	196.89
669	202.52
717	206.78

The data in Table 7 is plotted from 96 mmHg to 717 mmHg in figure 27. Where we can see an almost linear relation between the peak to peak signal and the pressure (particularly at the lower pressures below about 300 mmHg) as shown in figure 27.

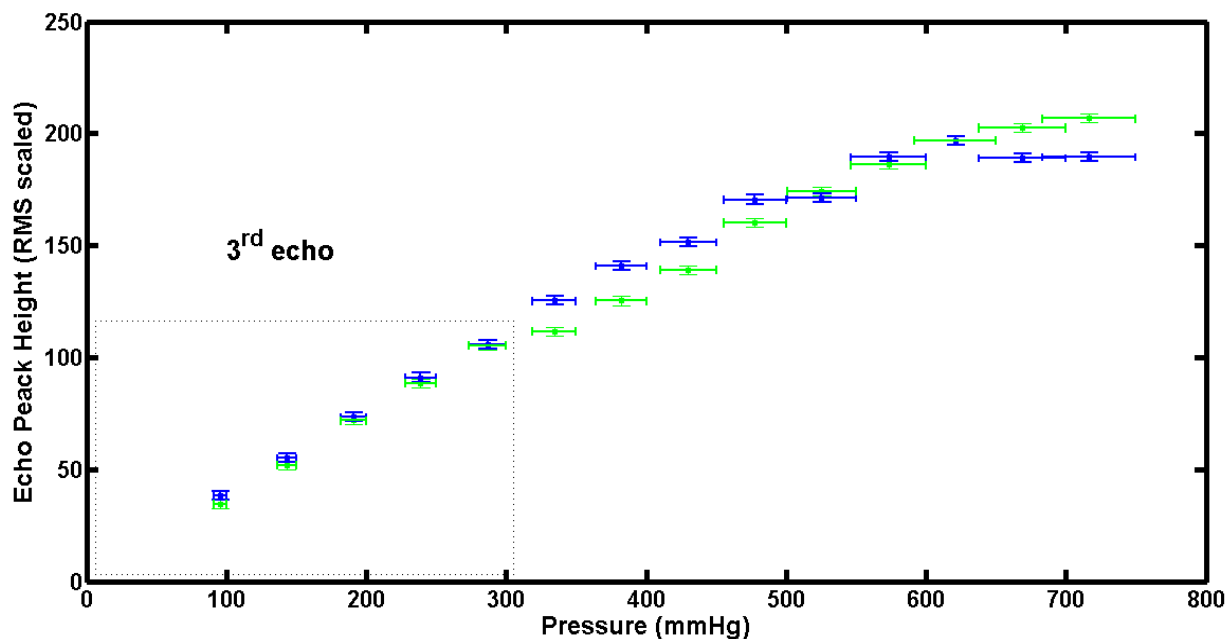


Figure 27. The change of the height of the third echo is plotted with respect to NO partial pressure. The model waveform is shown in green and the data waveform is shown in blue. The horizontal error-bars (green and blue) are taken as $\pm 5\%$ uncertainty in the pressure measurement, and the vertical error-bars are taken to cover our error in measuring the echo height. The dashed area identifies the linear region which is expanded and shown in figure 28.

The peak-to-peak height of the 3rd echo starts with a linear increase at lower pressure, and then it changes to be sub-linear at higher pressures. In order to find our limit of detection (the lowest detectable partial pressure of NO in our system), we extend the model waveform in the linear range to a horizontal value of 1 (which indicates the lowest experimental pressure we can expect to measure). Because the signal to noise ratio (SNR) is being plotted, a y-value of 1 indicates where our signal level drops to the noise level, and is identified as the limit of detection as shown in figure 28.

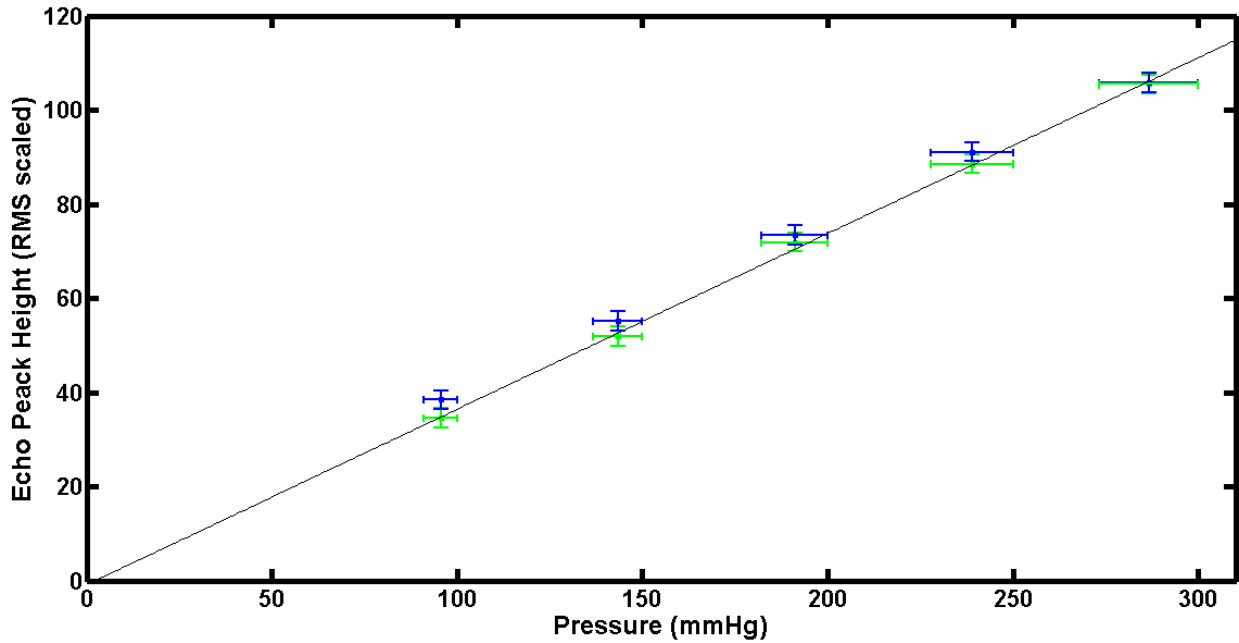


Figure 28. A plot of the inset of the earlier data points of figure 27, showing the extension of the model waveform (green dots) and data waveform (blue dots), with a linear fitting line (black). The horizontal error-bars (green and blue) are taken as $\pm 5\%$ uncertainty in the pressure measurement, and the vertical error-bars are taken to cover our error in measuring the echoes height

The measurements were obtained using a lock-in amplifier with time constant of 75 ms, and correspond to a total data collection time of approximately 35 minutes. The limit of detection (LOD) was found to be approximately 5 ± 0.3 mmHg, which translates to 6600 ± 400 ppm. However, this system is slow in comparison to commercially available THz systems that would actually be used for practical applications. We can therefore project what LOD is realistically achievable with commercially available systems by translating our SNR to that of other systems.

4.5 Future work

THz spectroscopy is increasing the opportunities for the spectroscopic studies of the chemical evolution of interstellar clouds. Both in absorption and emission, the detection limits for large molecules in the gas phase are expected to improve significantly, allowing the observations of more complex chemical species. In contrast to the power measurements typically made in the far-infrared for astronomical measurements, the advantage of using THz-TDS relies on its ability to study interaction between the THz field and specific molecules (in the wavelength range from 1 to 3 THz) directly in the time domain allowing the collection of vast amounts of data specific to the individual molecules.

On the other hand, the disadvantage of THz-TDS is poor detection limits compared to other techniques such as the use of QCL's and incoherent detection which can achieve tens of ppb. However, the use of commensurate echoes in the time domain for quantification and identification of gas species can be put into a practical context using current state-of-the art, commercially available THz time-domain spectrometers [1].

The fastest THz system commercially available is, the Advanced Photonix Inc. T-Ray 5000 system, which can produce 1000 THz waveforms every second with an 80 ps window and a signal to noise ratio approximately the same as what is measured here in 35 minutes.

Assuming measurements are made every minute (1000 waveforms/s x 60 s = 60,000 waveforms/min), and scaling the noise floor by the square root of the number of samples collected in one minute ($\sqrt{60,000} = 243$), This system would obtain a limit of detection of 0.025 mmHg or 33 ppm [1]. A sensitivity of 40 ppm is not enough for many applications, however, THz-TDS can perform in harsh environments with high temperatures and lots of particulate [51, 52].

The target of my thesis was to study pollutants that are emitted from bioenergy combustion systems, therefore, it is important to identify if THz-TDS is appropriate for real-time gas sensing and monitoring at different partial pressures. In particular, is THz-TDS a useful tool for characterizing gases in terms of performing the temporal sampling (time domain) instead of the traditional spectroscopy in the frequency domain.

We obtained a limit of detection of 6600 ± 400 ppm, which is large compared to the 10 ppm reported in a nitrogen atmosphere obtained by using the technique of quartz-enhanced photoacoustic spectroscopy [25]. However, projecting our LOD to what is expected using commercially available THz spectrometers (T-Ray 5000), we would expect a LOD of approximately 33ppm. Therefore, based on the present work, the expected LOD for our *new* technique of THz-TDS is competitive with other techniques in a nitrogen environment.

The advantage that THz-TDS has over other methods is that because of the coherent detection, it is insensitive to thermal background radiation which significantly complicates other spectroscopic methods in the far infrared from being useful in hot environments. Further, traditional IR ro-vibrational spectroscopy similarly is unsuitable to the harsh environments of combustion systems because it is strongly scattered by particulate making quantification and detection virtually impossible.

Combining these key benefits unique to THz-TDS with the fact that there are large concentrations of pollutant gasses in the combustion chamber, it becomes possible to implement this new technique within combustion systems for optimization and emissions monitoring. This is the area that is expected to benefit most from these types of measurements.

As additional future work, we would suggest using THz-TDS to study different types of pollution and gas streams in industrial gasification systems, such as: particulate matter, SO_x, NO_x, ash, smoke, VOCs.

Chapter 5

Conclusion

In conclusion, in this thesis we developed a theoretical model for the THz time-domain response of NO molecules and conducted a comparison to experimental measurements at different pressures to test the validity of the model. By fitting the model to our experimental data, we were able to extract experimental values of some physical parameters of NO. We obtained experimental values for the rotational constant, B_v , of the ground vibrational state, $v=0$. We were able to distinguish between the two different electronic state of Nitric Oxide (${}^2\Pi_{1/2}$ and ${}^2\Pi_{3/2}$) by getting two different values of the rotational constant, $B_0^{1/2}$ and $B_0^{3/2}$, both of which were found to be consistent with the published literature values.

From our time domain model of the THz response of NO, the distinguishable THz response that leads to the different measured values for the two electronic transitions of NO was manifest by a separation of the commensurate echoes into two distinct echoes at longer time scales, reflecting the larger amount of information carried in the shape of the time-domain waveforms.

We obtained an experimental value for the centrifugal distortion constant D_v for the ground vibrational state, $v = 0$, of each electronic state of NO (${}^2\Pi_{1/2}$ and ${}^2\Pi_{3/2}$), $D_0^{1/2}$ and $D_0^{3/2}$, at an atmospheric total pressure of NO, which was subsequently assumed to be independent of NO partial pressure and fixed in value in our model. The experimental value obtained was found to be consistent with literature values for the centrifugal distortion constant.

Fitting the model to our experimental data, we were able to extract values for the angular frequency linewidth, $\Delta\omega$, (inversely proportional to the molecular collisional time τ_c). This angular frequency linewidth varied with NO partial pressure, while maintaining a total system pressure of 1 atm with (N₂) as expected. In particular, it varied from the air-broadened value at low NO partial pressure to the self-broadened value at large NO partial pressure, and the numerical values obtained were consistent with those reported in the HITRAN database.

Further, and importantly, we were able to distinguish between the two different electronic states of NO (${}^2\Pi_{1/2}$ and ${}^2\Pi_{3/2}$) by fitting two different values of the angular frequency linewidths in our model, $\Delta\omega_{1/2}$ and $\Delta\omega_{3/2}$, instead of just one $\Delta\omega$. In this case, it was observed that both are consistent with the published literature values in the HITRAN database, and also consistent with what is expected based on the molecular structure of NO in the different electronic states with respect to the collisional cross section.

All of these combined measurements indicate that our model is appropriate, and useful to extract physical properties of a sample of NO gas in an N₂ environment, consistent with the excellent fitting of our model to the experimental data in the time domain. The confidence in the model then allows us to determine the limit of detection for NO molecules at atmospheric pressure to answer the objective question of this thesis, which is whether or not THz time-domain spectroscopy can be useful for emissions monitoring in an industrial setting.

We obtained a high limit of detection of 6600 ± 400 ppm, however, this was projected to be much lower for fast, commercially available systems (33 ppm). The advantages of using THz-TDS are that it can perform in harsh environments at high temperatures because it is insensitive to thermal background and it is insensitive to even large particulate matter because of the long wavelengths. Furthermore, it gives a lot of information about the chemical composition of the gases (which agree with the literature values).

In summary, my thesis contributes a theoretical model of the interaction of a THz field with NO molecules, allowing the response to be predicted in the time domain. The results give excellent agreement with experiment, and was used to extract values for the physical parameters of NO which are consistent with published literature values. Finally, we obtained a limit of detection of 6600 ± 400 ppm, which is projected to yield a LOD of a few tens of ppm with commercially available fast THz spectrometers, useful for quantification and spectroscopy in harsh environments where other technologies are problematic.

References

- [1] Patrick Kilcullen, I. D. Hartley, E. T. Jensen and M. Reid, "Terahertz Time Domain Gas-phase Spectroscopy of Carbon Monoxide," *Journal of Infrared, Millimeter and Terahertz Waves*, **36**, 380-389, (2015).
- [2] D. Grischkowsky, S. Keiding, Martin van Exter and Ch. Fattinger, "Far-Infrared Time-Domain Spectroscopy with Terahertz Beams of Dielectrics and Semiconductors," *Journal of the Optical Society of America B*, **7**, 2006-2015, (1990).
- [3] Ted M. Dawson and Solomon H. Snyder, "Gases as Biological Messengers: Nitric Oxide and Carbon Monoxide in the Brain," *Journal of Neuroscience*, **14** (9), 5147-5159, (1994).
- [4] K. Dormanns, R. G. Brown, T. David, "The role of nitric oxide in neurovascular coupling," *Journal of Theoretical Biology* **394**, 1-17, (2016).
- [5] Holger S. P. Muller, Kaori Kobayashi, Kazumasa Takahashi, Kazuko Tomaru, and Fusakazu Matsushima, "Terahertz spectroscopy of N¹⁸O and isotopic invariant fit of several nitric oxide isotopologs," *Journal of Molecular Spectroscopy*, 1-8, (2014).
- [6] T. Sivasakthivel, and K. K. Siva Kumar Reddy, "Ozone Layer Depletion and Its Effects: A Review," *International Journal of Environmental Science and Development*, **2** (1), 30-37, (2011)
- [7] Robert J. Blaszczak, "Nitrogen Oxides (NO_x), Why and how they are controlled," Office of air quality planning and standards (OAQPS), U.S. environmental protection agency, (1999). Retrieve March 2016, available: <https://www.epa.gov/ttn/catc1/dir1/fnoxdoc.pdf>
- [8] C. Leng, Q. Zhang, D. Zhang, C. Xu, T. Cheng, R. Zhang, J. Tao, J. Chen, S. Zha, Y. Zhang, X. Li, L. Kong, and W. Gao, "Variations of cloud condensation nuclei (CCN) and aerosol activity during fog-haze episode: a case study from Shanghai," *Atmospheric Chemistry and Physics*, **14**, 12499-12512, (2014).

- [9] Allan L. L. East, "The 16 valence electronic states of nitric oxide dimer (NO)₂," *The Journal of Chemical Physics*, **109**, 2185-2193, (1998).
- [10] Martin van Exter, Ch. Fattinger, and D. Grischkowsky, "Terahertz time-domain spectroscopy of water vapour," *Optics Letters*, **14** (20), 1128-1130, (1989).
- [11] Paolo G. Favero, Anna M. Mirri, and Walter Gordy, "Millimeter-wave Rotational Spectrum of NO in the ²Π_{3/2} state," *Physical Review*, **114**, 1534-1537, (1959).
- [12] Richard M. Neumann, "High-Precision radiofrequency spectrum of ¹⁴N¹⁶O," *The Astrophysical Journal*, **161**, 779-784, (1970).
- [13] Evan M. Hetrick and Mark H. Schoenfish, "Analytical Chemistry of Nitric Oxide," *Annual Review of Analytical Chemistry*, **2**, 409-433, (2009).
- [14] L. B. Kreuzer and C. K. N. Patel, "Nitric Oxide Air Pollution: Detection by Optoacoustic Spectroscopy," *Science*, **173**, 45-47, (1971).
- [15] András Miklós, Stefan Schäfer and Peter Hess, "Photoacoustic Spectroscopy, Theory," in *Encyclopedia of Spectroscopy and Spectrometry*, **2**, 1815-1822, (1999).
- [16] Samara L. Firebaugh, Klavs F. Jensen, and Martin A. Schmidt, "Miniaturization and integration of photoacoustic detection with a microfabricated chemical reactor system," *Journal of Microelectromechanical Systems*, **10** (2), (2001).
- [17] M. G. Allen, B. L. Upschulte, D. M. Sonnenfroh, W. T. Rawlins, C. Gmachl, F. Capasso, A. Hutchinson, D. Sivco, and A. Cho," Infrared characterization of particulate and pollutant emissions from gas turbine combustors," *The American Institute of Aeronautics and Astronautics (AIAA)*, (2001).
- [18] Bradley Ferguson, and X. Cheng Zhang, "Materials for terahertz science and technology," *Nature Materials*, **1**, 26-33, (2002).

- [19] Robinson JK, Bollinger MJ, and Birks JW, "Luminol/H₂O₂ chemiluminescence detector for the analysis of nitric oxide in exhaled breath," *Journal of Analytical Chemistry*, **71** (22), 5131-5136, (1999).
- [20] Elisabeth planchet and Werner M. Kaiser, "Nitric oxide (NO) detection by DAF fluorescence and chemiluminescence: a comparison using abiotic and biotic NO sources," *Journal of Experimental Botany*, **57** (12), 3043-3055, (2006)
- [21] V. Spagnolo, A. A. Kosterev, L. Dong, R. Lewicki, and F. K. Tittel, "NO trace gas sensor based on quartz-enhanced photoacoustic spectroscopy and external cavity quantum cascade laser," *Applied Physics B*, **100**, 125-130, (2010).
- [22] Rafal. Lewicki, J. H. Doty, R. F. Curl, F. K. Tittel, and G. Wysocki, "Ultrasensitive detection of nitric oxide at 5.33 μm by using external cavity quantum cascade laser-based Faraday rotation spectroscopy," *Proceedings of the National Academy of Sciences (PNAS)*, **106** (31) ,12587-12592, (2009).
- [23] Chad Roller, K. Namjou, J. D. Jeffers, M. Camp, A. Mock, P. J. McCann, J. Grego, " Nitric oxide breath testing by tunable-diode laser absorption spectroscopy: application in monitoring respiratory inflammation," *Applied Optics*, **41** (28), 6018-6029, (2002).
- [24] Angela Elia, C. D. Franco, P. M. Lugarà, and G. Scamarcio, "Photoacoustic Spectroscopy with Quantum Cascade Lasers for Trace Gas Detection," *Sensors*, **6** (10), 1411-1419, (2006).
- [25] Stuart Gray, Anping Liu, Feng Xie and Chung-en Zah, "Detection of nitric oxide in air with a 5.2 μm distributed-feedback quantum cascade laser using quartz-enhanced photoacoustic spectroscopy," *Optics Express*, **18** (22), 23357, (2010).
- [26] D. M. Mittleman, M. Gupta, R. Neelamani, R. G. Baraniuk, J. V. Rudd, and M. Koch, "Recent Advances in terahertz imaging," *Applied Physics B*, **68**, 1085-1094, (1999).

- [27] H. Harde, R. A. Cheville, and D. Grischkowsky, "Terahertz Studies of Collision-Broadened Rotational Lines," *The Journal of Physical Chemistry A*, **101**, 3646-3660, (1997).
- [28] D. H. Auston and K. F. Cheung, "Coherent time-domain far-infrared spectroscopy; Direct laser generation of 27-FSEC ultrashort optical pulses" *Optics and Photonics News*, **2**, 606-612, (1985).
- [29] J. Heyman, N. Coates, A. Reinhardt, and G. Stresser, "Diffusion and drift in terahertz emission at GaAs surfaces," *Applied Physics Letters*, **83** (2), 5476-5478, (2003).
- [30] Suranjana Sengupta, "Characterization of terahertz emission from high resistivity Fe-doped bulk Ga_{0.69}In_{0.31} as based photoconducting antennas," *Ph.D research*, Springer thesis, (2011)
- [31] M. Bass, P. A. Franken, J. F. Ward, and G. Weinreich, "Optical Rectification," *Physical Review Letters*, **9** (11), 446-449, (1962).
- [32] D. Dragoman, and M. Dragoman, "Terahertz fields and applications," *Progress in Quantum Electronics*, **28**, 1-66, (2004).
- [33] N. Katzenellenbogen and D. Grischkowsky, "Efficient generation of 380 fs pulses of THz radiation by ultrafast laser pulse excitation of a biased metal-semiconductor interface", *Applied Physics Letters*, **58** (3), 222-224, (1991)
- [34] Ch. Fattinger, D. Grischkowsky, "Terahertz beams," *Applied Physics Letters*, **54** (6), 490-492, (1989).
- [35] D. M. Mittleman, R. H. Jacobsen, R. Neelamani, R. G. Baraniuk, and M. C. Nuss, "Gas sensing using terahertz time-domain spectroscopy," *Applied Physics B*, **67**, 379-390, (1998).
- [36] H. Harde, S. Keiding, and D. Grischkowsky, "THz Commensurate Echoes: Periodic rephasing of molecular transitions in free-induction decay," *Physical Review Letters*, **66** (14), (1991).

- [37] Theodore E. Brown, H. Eugene LeMay, Bruce E. Bursten, Catherine Murphy, and Patrick Woodward, "Molecular Geometry and Bonding Theories," in *Chemistry: The Central Science*, **11**, 368-381, (2009).
- [38] Paul A. Tripler, A. Ralph, A. Llewlllyn, "Molecular Structure and Spectra" in *Modern Physics*, **5**, 363-395, (2008).
- [39] J. H Van Vleck, V. F. Weisskopf, "On the Shape of Collision-Broadened Lines," *Reviews of Modern Physics*, **17** (2), 227-236, (1945).
- [40] H. A. Lorentz, "The absorption and emission lines of gaseous bodies," Huygens Institute-Royal academy of science, **8**, 591- 611, (1906).
- [41] Hermann Harde, Daniel Grischkowsky, "Molecular Response Theory in Terms of the Uncertainty Principle," *The Journal of Physical Chemistry A*, **119**, 9085-9090, (2015).
- [42] H. Harde and D. Grischkowsky, "Coherent transients excited by subpicosecond pulses of terahertz radiation," *Journal of the Optical Society of America B*, **8**, 1642-1651, (1991).
- [43] M. D. Olman, M. Dominic McNelis, C. D. Hause, "Molecular constants of nitric oxide from the near infrared spectrum," *Journal of Molecular Spectroscopy*, **14** (1-4), 62-78 (1964).
- [44] Yong-Ge Lin, Jorge E. Colón-García, Carlos R. Cabrera, and Edwin Quiñones, "Rotational structure of a super-excited state of the NO molecule revealed by OODR-multiphoton laser spectroscopy," *The Journal of Physical Chemistry A*, **113** (42), 11262-11265, (2009).
- [45] Richard T. Hall and Jerome M. Dowling, "Pure Rotational Spectrum of Nitric Oxide," *The Journal of Chemical Physics*, **45** (6), 1899-1903, (1966).
- [46] Chakree Tanjaroon, Scott W. Reeve, Alan Ford, W. Dean Murry, Kevin Lyon, Bret Yount, Dan Britton, William A. Burns, Susan D. Allen, and J. Bruce Johnson, "Picosecond rotationally resolved stimulated emission pumping spectroscopy of nitric oxide," *The Journal of Chemical Physics*, **393**, 80-85, (2012).

- [47] J. Danielak, U. Domin, R. Kepa, M. Rytel, and M. Zachwieja, "Reinvestigation of the Emission γ Band System ($A^2\Sigma^+ - X^2\Pi$) of the NO Molecule," *Journal of Molecular Spectroscopy*, **181**, 394-402, (1997).
- [48] L.S. Rothman, I. E. Gordon, Y. Babikov, A. Barbec, D. Chris Benner, P. F. Bernath, M. Birk, L. Bizzocchi, V. Boudon, L. R. Brown, A. Campargue, K. Chance, E. A. Cohen, L. H. Coudert, *High-resolution transmission molecular absorption database (HITRAN)*, Retrieved February, 2017, Available: <http://www.hitran.org>.
- [49] David R. Lide, "Spectroscopic constants of Diatomic Molecules," in *Handbook of Chemistry and Physics*, CRC Press, **48**, 105-106, (2004).
- [50] Erhard W. Rothe and Richard B. Bernstein, "Total collision cross sections for the interaction of atomic beams of alkali metals with gases," *The Journal of Chemical Physics*, **31** (6), (1959).
- [51] R. Cheville and D. Grischkowsky, "Far-infrared terahertz time-domain spectroscopy of flames," *Optics Letters*, **20**, 1646-1648, (1995).
- [52] J. Bassi, M. Stringer, B. Miles, and Y. Zhang, "Terahertz time-domain spectroscopy of high-pressure flames," *Frontiers of Energy and Power Engineering in China* **3**, 123-133, (2014).
- [53] M. Reid, T. Inagaki, S. Tsuchikawa, K. Lawyer, B. Ahmed, A. Nasr Mohamed, E. T. Jensen, and I. D. Hartley, "Terahertz spectroscopy of wood and combustion gas," *Invited presentation at the Canadian Association of Physics Congress*, Sudbury, ON, CAN (Wednesday, June 18, 2014).
- [54] M. Reid, I. Hartley, E. Jensen, P. Kilcullen, B. Ahmed, A. Nasr Mohamed, and K. Lawyer, "THz NDE and applications for sensing and imaging of wood products," *Invited departmental seminar, Graduate Agricultural School, Nagoya University, Japan* (Nov. 4, 2016).

Appendix

Appendix A. (Statistical error analysis)

In order to estimate the error associated with the random electrical noise in our system, which fundamentally limits the signal-to-noise ratio (SNR) in this work, we first calculate the sum of squared residuals S , as the difference between experimental values and the model at the i^{th} time point as S_i . The sum of squared residuals, S , is then given by:

$$S = \sum_{i=1}^n S_i^2 \quad (1)$$

Here, we assume that S is represented by a normal distribution is therefore represented by a normal random variable $X \sim N(\mu, \sigma^2)$.

We define the statistic T representing the above sum of squared residuals with the addition of n random variables, Z_i , each normally-distributed with mean equal to μ and variance σ^2 : $T \sim N(\mu, \sigma^2)$

$$T = \sum_{i=1}^n (S_i + Z_i)^2 = \sum_{i=1}^n S_i^2 + 2 \sum_{i=1}^n S_i Z_i + \sum_{i=1}^n Z_i^2 \quad (2)$$

By substituting the value of S from equation (1) into equation (2), we get:

$$T = \sum_{i=1}^n (S_i + Z_i)^2 = S + 2 \sum_{i=1}^n S_i Z_i + \sum_{i=1}^n Z_i^2 \quad (3)$$

The first term of equation(3) is computed from our data and our model, so it should give a constant value of S , and the 2nd term is the sum of normal random variables, so it has a normal distribution given by:

$$2 \sum_{i=1}^n S_i Z_i : N \left(0, \sigma^2 \sum_{i=1}^n (2S_i)^2 \right) = N (0, 4\sigma^2 S) \quad (4)$$

Finally, the 3rd term of equation (3), which is represented by a sum of squared independent variables, which is approximately constant for large n and can be determined by the measured Root Mean Square (*RMS*) noise floor of our signals:

$$(RMS)^2 \approx \frac{1}{n} \sum_{i=1}^n Z_i^2 \quad (5)$$

In other words, we take the RMS noise floor to be an estimate of the standard deviation parameter of the normally distributed Z_i and justify this view by the above equation (the R.H.S. is the biased estimator for σ^2). Thus the statistic T has essentially a normal distribution:

$$T : N (S + n(RMS)^2, 4\sigma^2 S) \quad (6)$$

Thus, we can estimate the error in our best fitting results, where we plot the sum of squared residuals S as a function of the fitting parameter about a global minima, along with upper and lower curves corresponding to $\pm 1\sigma$ confidence intervals. This is shown in figure 15, which was used to extract the error bounds for the parameters estimated by minimizing the SSE.